Research Square

Preprints are preliminary reports that have not undergone peer review.
They should not be considered conclusive, used to inform clinical practice,
or referenced by the media as validated information.

Hydrochemical evolution and formation mechanisms of geothermal systems across contrasting tectonic settings in Tibet, China

Junjie Ba
Institute of Karst Geology, CAGS/ Key Laboratory of Karst Dynamics, MNR & GZAR
Qingyu Zhang
karstzhangqy@163.com

Institute of Karst Geology, CAGS/ Key Laboratory of Karst Dynamics, MNR & GZAR
Guoquan Nie
Institute of Karst Geology, CAGS/ Key Laboratory of Karst Dynamics, MNR & GZAR
Shaochong Ji
Institute of Karst Geology, CAGS/ Key Laboratory of Karst Dynamics, MNR & GZAR
Zhen Li
Institute of Karst Geology, CAGS/ Key Laboratory of Karst Dynamics, MNR & GZAR

Research Article

Keywords: Tibetan Plateau, geothermal water, hydrogen and oxygen isotopes, hydrochemical evolution, formation mechanisms

Posted Date: November 11th, 2026

DOI: https://doi.org/10.21203/rs.3.rs-11533319/v1

License: This work is licensed under a Creative Commons Attribution 4.0 International License.
Read Full License

Additional Declarations: No competing interests reported.

Hydrochemical evolution and formation mechanisms of geothermal systems across contrasting tectonic settings in Tibet, China

Junjie Ba [1,2], Qingyu Zhang [1,2]*,Guoquan Nie, Shaochong Ji, Zhen Li

[1] Institute of Karst Geology, CAGS/ Key Laboratory of Karst Dynamics, MNR & GZAR, Guilin, 541004, China;
[2] International Research Center on Karst under the Auspices of UNESCO, National Center for International Research on Karst Dynamic System and Global Change, Guilin541004, China
* Correspondence: karstzhangqy@163.com

The Tibetan Plateau lies within the India–Eurasia collision zone and contains abundant geothermal resources with pronounced regional differences in formation mechanisms. Comparisons of geothermal system genesis across Tibetan tectonic units remain limited. Hydrochemical and isotopic analyses, geothermometry, and silica–enthalpy mixing models were applied to Longmu Co, Doma, and Yangbajing. The integrated dataset was used to identify principal recharge sources, assess reservoir water–rock equilibrium, and develop regional conceptual models of geothermal fluid circulation. Longmu Co waters in northern Qiangtang are of the Cl·HCO_3–Na·Ca type, mainly reflecting carbonate and evaporite dissolution. Doma waters in southern Qiangtang are predominantly HCO_3–Na, controlled by water–rock interaction and cation exchange. Yangbajing waters in the Lhasa terrane are Cl·HCO_3–Na, influenced by silicate and evaporite dissolution. Meteoric water supplies all three systems. Longmu Co receives recharge from surrounding mountains; Doma receives distant high-elevation precipitation and snow and ice meltwater. Yangbajing receives precipitation and meltwater from the Nyainqentanglha Mountains. Estimated recharge elevations are 5236–5497, 6240–6362, and 5086–5436 m at Longmu Co, Doma, and Yangbajing, respectively. Corresponding circulation depths are 5047–6806, 6653–7294, and 4867–5345 m. Reservoir temperatures are 145–196, 175–192, and 225–247 °C, and cold-water mixing fractions are 51–61%, 57–63%, and 66–69%, respectively. Doma also shows a possible deep magmatic fluid signal. Conceptual models indicate a shared deep thermal background but contrasting heat-source mechanisms. Yangbajing is sustained primarily by intracrustal magma chambers; Doma and Longmu Co reflect mantle heat flow and localized intracrustal melts under differing structural controls. These comparisons inform geothermal exploration and resource assessment in high-elevation collisional orogens.

Keywords: Tibetan Plateau; geothermal water; hydrogen and oxygen isotopes; hydrochemical evolution; formation mechanisms

1 Introduction

As a core component of the Mediterranean–Himalayan geothermal belt (Guo et al. 2007), the Tibetan Plateau has undergone intense crustal uplift and deep tectonic modification during continued continent–continent collision and orogenesis between the Indian and Eurasian plates. It is among the most active regions globally in terms of

crustal thermal evolution and deep fluid activity. Its intricate fault systems provide favorable pathways for hydrothermal circulation. Meanwhile, collision-induced crustal thickening, partial melting, and the upwelling of hot mantle material provide substantial deep heat for geothermal systems (Huang et al. 2026; Zhang et al. 2024). Together, these conditions favor widespread hydrothermal activity across the region (Elenga et al. 2021). Tibet consequently hosts some of the most abundant high-temperature geothermal resources in China. Its intense hydrothermal activity and diverse geothermal manifestations have substantial scientific and practical significance for understanding deep geological processes, constraining fluid evolution mechanisms, and developing geothermal energy as a clean energy resource. Accordingly, the scientific assessment and sustainable development of geothermal resources in Tibet have attracted considerable research attention (Olasolo et al. 2016).

Tibet comprises tectonic terranes of different geological ages and origins. Large differences in basement lithology, host-rock composition, tectonic activity, and near-surface geological conditions have produced contrasting mechanisms of geothermal fluid formation and pathways of fluid evolution. Existing research on geothermal fluids in Tibet has mainly focused on detailed investigations of well-known high-temperature geothermal fields, such as Yangbajing, Daggyai, and Gulu (Wang et al. 2021; Zhou et al. 2023). Most studies have examined individual local systems, whereas large-scale comparisons across different tectonic units from northern to southern Tibet are lacking. Differences in the controls on heat supply and the evolution of fluids among geothermal systems in different terranes remain unresolved, limiting a comprehensive understanding of the regional controls on geothermal reservoir formation across the Tibetan Plateau.

To address these limitations, three typical geothermal systems spanning southern to northern Tibet were selected: Yangbajing in the Gangdese belt of the Lhasa terrane, Doma in the southern Qiangtang depression, and Longmu Co in the northern Qiangtang depression. Geothermal water samples were collected, and hydrochemical characterization, multivariate statistical analysis, hydrogen and oxygen isotope tracing, and geochemical geothermometry were integrated to investigate hydrochemical evolution, recharge and circulation pathways, and deep reservoir characteristics in different tectonic units. The principal mechanisms governing geothermal system formation under different tectonic settings were thereby elucidated. The results provide a theoretical and scientific basis for geothermal exploration, resource assessment, and sustainable development in tectonically complex regions of the Tibetan Plateau.

2 Geological and geothermal setting

Three areas with geothermal manifestations, Yangbajing, Longmu Co, and Doma, were selected for this study. They lie within the Gangdese belt of the Lhasa terrane, the northern Qiangtang depression, and the southern Qiangtang depression, respectively, and exhibit marked differences in their geothermal geological characteristics.

The Yangbajing geothermal field is located in Damxung County, Lhasa. Tectonically, it lies north of the Yarlung Zangbo suture and the mantle suture of the

Tibetan Plateau and is controlled by the intersection of the approximately north–south-trending Yadong–Gulu rift and the northeast-trending Nyainqentanglha piedmont fault. The deep basement consists mainly of Precambrian to Paleozoic metamorphic rocks of the Nyainqentanglha Group and Cretaceous to Paleocene intermediate–felsic intrusions of the Gangdese belt. It is overlain by unconsolidated Quaternary glacial, alluvial, and proluvial deposits ranging from several meters to several hundred meters in thickness (Kapp et al. 2008; Tan et al. 2014). The deep reservoirs occur in fractured granitic and metamorphic rocks, and drilling has encountered temperatures of 270 °C below a depth of 1200 m (Lei et al. 2023). Hydrothermal activity is intense, with widespread geothermal manifestations including boiling springs, thermal lakes, fumaroles, and diffuse soil microseepage (Su et al. 2020; Yu et al. 2022). Compression associated with plate collision has caused crustal thickening and partial melting. Geophysical investigations have revealed a low-velocity, highly conductive layer at depths of 15–20 km. It is generally interpreted as a magma chamber containing residual crustal or mantle melt and providing a stable intracrustal heat source for the region (Brown et al. 1996; Wei et al. 2001; Zhang et al. 2017). Geothermal fluids are recharged mainly by snow and ice meltwater and meteoric water from the Nyainqentanglha Mountains. They circulate deeply along faults and fractures, are heated by magma chambers, and acquire gaseous components released during crustal melting. The heated fluids migrate upward and accumulate in fractured reservoirs before rising through fault conduits into the shallow subsurface, mixing with cold water, and discharging at the surface as hot springs (Wang et al. 2024). Previous studies indicate that the Yangbajing geothermal field contains multiple vertically distributed high-temperature reservoirs at different depths. These reservoirs are closely interconnected and form part of the same hydrothermal system (Wang et al. 2022).

The Qiangtang Basin lies between the Hoh Xil–Jinsha River and Bangong Co–Nujiang sutures. Extending approximately 1200 km from east to west and more than 300 km from north to south, it is the largest composite Mesozoic continental–marine sedimentary basin in China (Cao et al. 2020). Its marine sedimentary succession, deposited from the Late Triassic to the Early Cretaceous, exceeds 5000 m in cumulative thickness (Liu et al. 2020). Tectonically, the basin belongs to the Qiangtang block, where east–west extension has produced a series of normal faults and conjugate strike-slip faults (Yin and Taylor 2011). The Longmu Co–Shuanghu suture divides the Qiangtang block into the southern and northern Qiangtang depressions. Some studies have proposed mantle-plume uplift beneath northern Qiangtang during the rapid regional uplift of the Tibetan Plateau in the Quaternary (Liu et al. 2024). Shallow to intermediate-depth thrust faults in the southern Qiangtang depression are predominantly oriented approximately east–west. Faults in the central and southern parts of northern Qiangtang mainly trend north-northwest, changing to east–west farther north (Wang et al. 2019). Crustal zones of weakness formed by these major deep faults and associated secondary faults provide preferential pathways for the upward migration of deep thermal fluids and the development of surface hydrothermal activity. The Qiangtang Basin has undergone multiple stages of tectonic evolution and preserves

evidence of Cenozoic magmatism (Liu et al. 2024). Previous studies have identified widespread low-velocity bodies within the crust beneath the basin and an 18-km Moho offset beneath the central uplift, suggesting the possible presence of partial melts or conduits for the upward transfer of mantle heat (Liu et al. 2026; Wang et al. 2016; Zhang et al. 2012). In addition, CO_2 in the region exhibits a pronounced mixed crustal–mantle origin, and $^3He/^4He$ ratios are markedly higher than those of typical crustal fluids, indicating a contribution from deep mantle-derived volatiles. Three-dimensional magnetotelluric inversion further indicates that the formation of the Doma geothermal system is associated with the upwelling of deep hot material along ancient sutures, faults, and other weak, fractured zones (Kapp et al. 2000; Wang et al. 2023; Zhang et al. 2012). Terrestrial heat-flow values in the Qiangtang Basin mainly range from 43.0 to 98.5 mW/m², and geothermal gradients range from 2.5 to 2.9 °C/100 m (Zhang et al. 2011; Zhao et al. 1998). This elevated deep thermal regime provides a sustained present-day heat source for the geothermal systems.

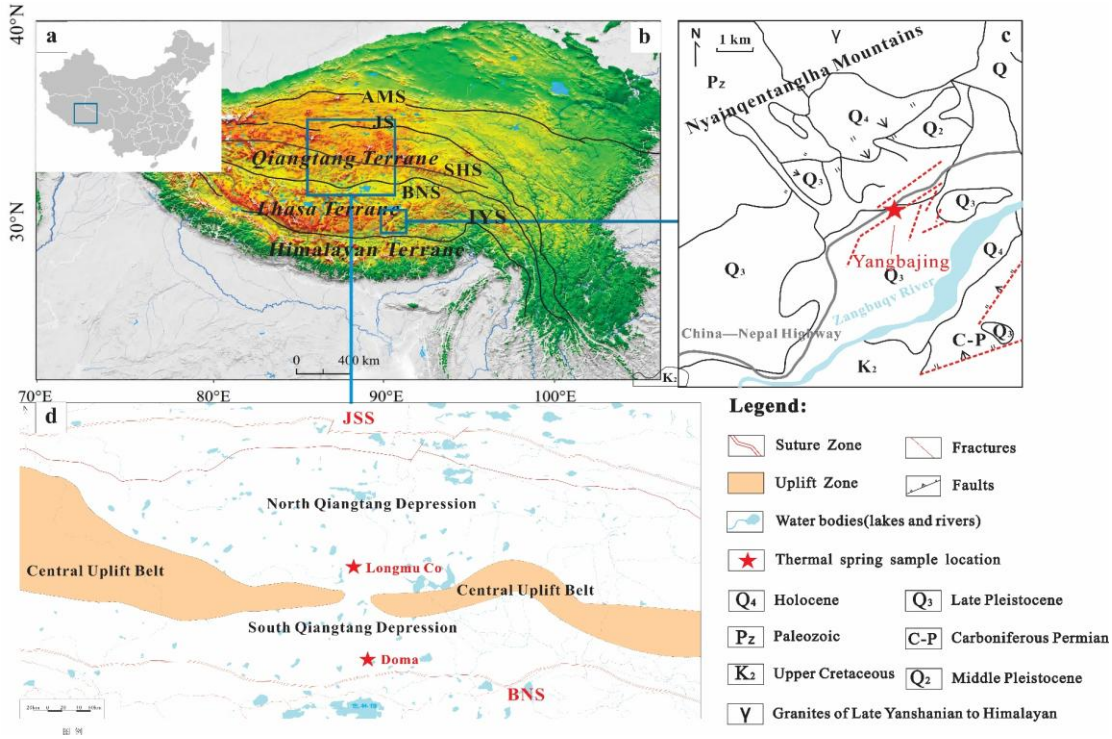


Fig. 1 a Location of the Tibet Autonomous Region, China; b simplified tectonic map of the Himalayan–Tibetan orogenic belt (suture abbreviations: AMS, Anyimaqen–Kunlun–Muztagh suture; JS, Jinsha River suture; SHS, Longmu Co–Shuanghu suture; BNS, Bangong Co–Nujiang suture; IYS, Indus–Yarlung Zangbo suture); c geological and tectonic map of Yangbajing showing the sampling locations; d geological and tectonic map of the Qiangtang region showing the sampling locations. The Chinese labels in panel d denote Siling Co and the legend

Doma is situated in the southern Qiangtang depression, within a tectonically sensitive zone north of the Bangong Co–Nujiang suture. The southern Qiangtang block mainly comprises two stratigraphic assemblages: Cambrian–Silurian weakly metamorphosed limestone, sandstone, and slate, and Carboniferous–Permian sedimentary rocks interbedded with mafic volcanic rocks (Zhang et al. 2012). The Bangong Co–Nujiang suture is characterized by intense tectonic mixing and contains

abundant ophiolites, Late Cretaceous to Cenozoic intermediate–felsic intrusions, and volcanic rocks. Longmu Co lies within the northern Qiangtang depression, along the margin of the Shuanghu–Longmu Co Cenozoic active fault zone. Its regional tectonic architecture is dominated by graben and half-graben systems formed under extension. The main lithologies are sandstone, siltstone, mudstone, and carbonate rocks, with the surface covered by unconsolidated Quaternary lacustrine, alluvial, and proluvial deposits (Yin and Harrison 2000; Zhang et al. 2012).

3 Materials and methods

3.1 Sampling and analysis

Geothermal water samples were systematically collected from the Qiangtang and Yangbajing regions of Tibet in 2025. To ensure sample representativeness, all water samples were collected at outlets with stable discharge. All sampling and analytical procedures strictly followed the Code for Geological Exploration of Geothermal Resources (GB/T 11615—2010). Before sampling, the geographical coordinates, elevation, and other location information for each sampling site were recorded using a handheld GPS receiver. Geothermal water pH, temperature (T), and total dissolved solids (TDS) were measured in situ using a portable multiparameter water-quality meter. High-density polyethylene sampling bottles were rinsed 3–4 times with the water to be sampled, and separate aliquots were collected for different analyses. Samples for cation and SiO_2 analyses were filtered through 0.45-μm membrane filters and immediately acidified to pH < 2 using high-purity nitric acid to prevent cation hydrolysis and adsorption. Samples for anion analyses were filtered and directly transferred to separate bottles. Samples for hydrogen and oxygen isotope analyses were collected in completely filled bottles without air bubbles, and the bottle openings were immediately sealed with paraffin to prevent isotope fractionation caused by evaporation. All samples were labeled in the field, immediately stored in a vehicle-mounted refrigerator at 4 °C, and transported to the laboratory as soon as possible for analysis.

Comprehensive hydrochemical and isotopic analyses were conducted at the Institute of Karst Geology, Chinese Academy of Geological Sciences. The analytical methods and instruments are listed in Table 1. Major cations and dissolved silica were determined using inductively coupled plasma optical emission spectrometry, whereas the principal anions were measured by ion chromatography. Bicarbonate and carbonate were determined in the field by double-indicator titration. The analytical results were subsequently assessed using the percentage ionic charge-balance error. All charge-balance errors were within ±5%, indicating reliable analytical quality and suitability for subsequent hydrochemical investigation. Stable hydrogen and oxygen isotopes (δD and $\delta^{18}O$) were measured using a liquid-water isotope analyzer, and the results are reported relative to V-SMOW. Dissolved inorganic carbon isotopes ($\delta^{13}C_{DIC}$) were measured using gas isotope ratio mass spectrometry, and ^{3}H was determined using an ultra-low-background liquid scintillation spectrometer.

Table 1 Major water-quality parameters of geothermal fluids and analytical methods

No.	Parameter	Unit	Setting	Analytical method and instrument
1	pH	None	Field	Portable multiparameter water-quality analyzer (AQUAREAD AP700)
2	T	°C	Field	Portable multiparameter water-quality analyzer (AQUAREAD AP700)
3	TDS	mg/L	Field	Portable multiparameter water-quality analyzer (AQUAREAD AP700)
4	Ca^{2+}	mg/L	Lab	Inductively coupled plasma optical emission spectrometer (iCAP 6300)
5	K^{+}	mg/L	Lab	Inductively coupled plasma optical emission spectrometer (iCAP 6300)
6	Na^{+}	mg/L	Lab	Inductively coupled plasma optical emission spectrometer (iCAP 6300)
7	Mg^{2+}	mg/L	Lab	Inductively coupled plasma optical emission spectrometer (iCAP 6300)
8	SiO_2	mg/L	Lab	Inductively coupled plasma optical emission spectrometer (iCAP 6300)
9	HCO_3^{-}	mg/L	Field	Double-indicator titration
10	CO_3^{2-}	mg/L	Field	Double-indicator titration
11	Cl^{-}	mg/L	Lab	Ion chromatograph (DIONEX ICS-2100)
12	SO_4^{2-}	mg/L	Lab	Ion chromatograph (DIONEX ICS-2100)
13	F^{-}	mg/L	Lab	Ion chromatograph (DIONEX ICS-2100)
14	δD	‰	Lab	Liquid-water isotope analyzer (L2130-i)
15	$\delta^{18}O$	‰	Lab	Liquid-water isotope analyzer (L2130-i)
16	^{3}H	TU	Lab	Ultra-low-background liquid scintillation spectrometer (Quantulus 1220)
17	$\delta^{13}C_{DIC}$	‰	Lab	Gas isotope ratio mass spectrometer (253 Plus)

3.2 Data processing

3.2.1 Saturation indices

The geochemical software PHREEQC 3.8.6 was used to calculate the saturation indices (SI) of representative minerals in each group of geothermal water samples. An SI of 0 indicates that the water is saturated with respect to the mineral and that dissolution and precipitation are at equilibrium. An SI > 0 indicates supersaturation and the potential for precipitation, whereas an SI < 0 indicates undersaturation and a tendency for further dissolution (Ba et al. 2022).

3.2.2 Recharge elevation

The hydrogen and oxygen isotopic composition of precipitation exhibits a pronounced elevation effect (Han et al. 2024), whereby δD and $\delta^{18}O$ become systematically depleted with increasing elevation. Because δD in geothermal fluids is relatively resistant to exchange during high-temperature water–rock interaction at depth, it behaves comparatively conservatively. Stable isotope compositions can therefore be used to quantitatively estimate geothermal water recharge elevations and their ranges, using the following equation:

$$H = H_0 + \frac{\delta \mathrm{D}_{\mathrm{sample}} - \delta \mathrm{D}_0}{\mathrm{grad}} \quad (1)$$

where H is the inferred elevation of the recharge area (m); H_0 is the sampling-site elevation of each geothermal water sample (m); δD_{sample} is the measured hydrogen isotope composition of the geothermal water sample (‰); δD_0 is the reference hydrogen isotope composition of precipitation near the sampling site (‰); and grad is the isotope elevation gradient (‰/100 m).

3.2.3 Geothermometers

Cation geothermometers are based on the thermodynamics of cation-exchange reactions in water–rock equilibrium systems. They estimate reservoir temperatures using empirically calibrated relationships between geothermal fluid cation concentrations and temperature. Their reliability depends on the state of mineral equilibrium and the extent of water–rock reaction. The equations are as follows (Fournier and Potter 1979; Giggenbach 1988):

Na–K cation geothermometer:

$$T = \frac{1217}{\log\left(\frac{\mathrm{Na}}{\mathrm{K}}\right) + 1.483} - 273.15 \quad (2)$$

K–Mg cation geothermometer:

$$T = \frac{4410}{13.95 - \log\left(\frac{\mathrm{K}^2}{\mathrm{Mg}}\right)} - 273.15 \quad (3)$$

Silica geothermometers estimate reservoir temperatures from the temperature dependence of silica mineral solubility. Natural silica occurs in multiple mineral phases with substantially different solubility curves. The applicable silica geothermometer must therefore be selected by considering both mineral saturation states and the reservoir temperature range to obtain a reasonable estimate of the deep reservoir temperature. The equations are as follows (Arnórsson et al. 1983; Fournier 1977):

Quartz geothermometer with no steam loss:

$$T = \frac{1309}{5.19 - \log\left(\mathrm{SiO}_2\right)} - 273.15 \quad (4)$$

Quartz geothermometer with maximum steam loss:

$$T = \frac{1522}{5.75 - \log\left(\mathrm{SiO}_2\right)} - 273.15 \quad (5)$$

Chalcedony geothermometer with no steam loss:

$$T = \frac{1032}{4.69 - \log(\mathrm{SiO_2})} - 273.15 \tag{6}$$

Chalcedony geothermometer with maximum steam loss:

$$T = \frac{1112}{4.91 - \log(\mathrm{SiO_2})} - 273.15 \tag{7}$$

3.2.4 Silica–enthalpy mixing model

Fournier and Truesdell proposed the silica–enthalpy mixing model in 1974 (Fournier 1977; Fournier and Truesdell 1974). By simultaneously solving the SiO_2 concentration and enthalpy mixing equations for the cold-water endmember, mixed fluid, and unmixed thermal water, either graphically or iteratively, the original deep reservoir temperature and the cold-water mixing fraction can be determined together. The equations are as follows:

$$\begin{cases} X_c \cdot f + X_b \cdot (1-f) = X_m \\ H_c \cdot f + H_b \cdot (1-f) = H_m \end{cases} \tag{8}$$

where X_c is the enthalpy of the cold water (J/g); X_b is the initial enthalpy of the geothermal water (J/g); X_m is the final enthalpy of the mixed geothermal water (J/g); H_c is the SiO_2 concentration of the cold water ($mg \cdot L^{-1}$); H_b is the initial SiO_2 concentration of the geothermal water ($mg \cdot L^{-1}$); H_m is the SiO_2 concentration of the mixed geothermal water ($mg \cdot L^{-1}$); and f is the cold-water mixing fraction (%).

3.2.5 Circulation depth

Geothermal water in the study areas is recharged by meteoric water and snow and ice meltwater. After being heated during circulation, it rises and discharges at the surface as hot springs. Its circulation depth can be estimated from the geothermal gradient using the following equation:

$$Z = \frac{T - T_0}{G} + Z_0 \tag{9}$$

where Z is the thermal water circulation depth (m); Z_0 is the depth of the constant-temperature zone (m); T is the reservoir temperature (°C); T_0 is the long-term mean annual air temperature in the study area (°C); and G is the geothermal gradient (°C/km).

4 Results

4.1 Geothermal water chemistry

Geothermal water samples were collected from Longmu Co, Doma, and Yangbajing. Three samples were collected from Longmu Co and designated BQT01, BQT02, and BQT03; six samples were collected from Doma and designated NQT01, NQT02, NQT03, NQT04, NQT05, and NQT06; and six samples were collected from Yangbajing and designated YBJ01, YBJ02, YBJ03, YBJ04, YBJ05, and YBJ06. The descriptive statistics for the hydrochemical constituents (Table 2) reveal pronounced differences in temperature, mineralization, and ionic composition among geothermal

fluids from different tectonic belts across southern to northern Tibet. Spring discharge temperatures were relatively consistent within each study site, with coefficients of variation below 0.05. At Longmu Co, discharge temperatures ranged from 72 to 75 °C, with a mean of 73 °C and a coefficient of variation (CV) of 0.02. At Yangbajing, temperatures ranged from 74 to 80 °C, with a mean of 77 °C and a CV of 0.03. At Doma, geothermal water temperatures ranged from 68 to 75 °C, with a mean of 72.3 °C and a CV of 0.04. The pH values of geothermal waters at all three sites ranged from 7.2 to 8.7 and were relatively consistent, with coefficients of variation below 0.1, indicating generally weakly alkaline conditions. Geothermal water at Yangbajing was distinctly more alkaline than that at Longmu Co and Doma in the Qiangtang Basin, indicating differences in fluid formation and evolution and in the conditions under which the geothermal water is stored.

Total dissolved solids (TDS) concentrations in Doma geothermal water ranged from 2068.5 to 2186.0 mg/L, with a mean of 2125.7 mg/L. At Longmu Co, TDS concentrations ranged from 1066.0 to 1178.0 mg/L, with a mean of 1107.1 mg/L; at Yangbajing, they ranged from 1024.0 to 1402.0 mg/L, with a mean of 1221.3 mg/L. The substantially higher TDS concentrations at Doma indicate highly mineralized water and reflect differences among the three systems in reservoir host rocks and fluid evolution pathways. Doma is located within a sedimentary basin containing extensive Mesozoic marine sedimentary strata rich in soluble salts. Continued leaching of these salts during geothermal fluid circulation results in the markedly elevated TDS concentrations.

Silica concentrations in geothermal water at Longmu Co ranged from 60.1 to 101.2 mg/L, with a CV of 0.29. This substantial compositional variability suggests that the samples may originate from different reservoirs or may have undergone markedly different degrees of fluid mixing or water–rock interaction. Silica concentrations varied less at Doma and Yangbajing, with CVs below 0.1 at both sites. At Doma, concentrations ranged from 81.6 to 93.7 mg/L, with a mean of 87.1 mg/L; at Yangbajing, they ranged from 130.7 to 157.1 mg/L, with a mean of 140.5 mg/L. Silica is widely used in geothermometry because its solubility increases with temperature under water–rock equilibrium conditions. SiO_2 concentrations at Yangbajing were markedly higher than those in the two geothermal systems in the Qiangtang Basin. Assuming that water–rock equilibrium was attained in the reservoir and that no substantial SiO_2 precipitation occurred during ascent, this difference suggests that geothermal fluids at Yangbajing may have followed deeper circulation pathways and experienced silicate mineral dissolution at higher temperatures.

Table 2 Statistical summary of the chemical composition of geothermal water

		TDS	T	SiO_2	pH	K^+	Na^+	Ca^{2+}	Mg^{2+}	HCO_3^-	CO_3^{2-}	SO_4^{2-}	Cl^-	F^-
Longmu Co N=3	**Min**	1066.0	72.0	60.1	7.3	26.2	239.6	91.1	12.4	346.0	/	109.5	322.5	2.3
	Max	1178.0	75.0	101.2	7.9	36.3	269.1	94.7	12.8	369.4	/	114.4	350.9	3.2
	Mean	1107.1	73.0	76.1	7.5	30.0	257.3	92.8	12.7	360.9	/	112.4	332.2	2.6
	SD.	61.7	1.7	22.1	0.3	5.5	15.6	1.8	0.2	12.9	/	2.5	16.3	0.6
	Var.	3804.4	3.0	486.2	0.1	29.9	243.1	3.3	0.1	167.6	/	6.4	264.3	0.3
	CV	0.06	0.02	0.29	0.05	0.18	0.06	0.02	0.02	0.04	/	0.02	0.05	0.21
Doma N=6	**Min**	2068.5	68.0	81.6	7.2	45.5	717.0	33.2	7.8	1962.3	/	129.4	22.9	3.1
	Max	2186.0	75.0	93.7	7.6	53.1	764.3	62.2	8.2	2083.7	/	152.1	44.5	4.1
	Mean	2125.7	72.3	87.1	7.4	48.3	741.9	51.5	8.0	2013.8	/	139.2	28.4	3.4
	SD.	51.7	2.7	5.2	0.2	2.8	19.5	13.3	0.2	47.3	/	9.2	8.1	0.4
	Var.	2677.4	7.1	27.3	0.03	7.9	382.0	176.0	0.03	2236.8	/	84.5	65.3	0.1
	CV	0.02	0.04	0.06	0.02	0.06	0.03	0.26	0.02	0.02	/	0.07	0.28	0.11
Yangbajing N=6	**Min**	1024.0	74.0	130.7	7.8	41.5	292.8	3.6	0.0	159.2	0.0	35.8	266.0	9.9
	Max	1402.0	80.0	157.1	8.7	55.4	456.0	24.8	0.3	447.0	110.4	163.4	430.4	15.2
	Mean	1221.3	77.0	140.5	8.2	48.3	383.7	10.4	0.1	292.2	43.8	73.3	363.7	13.1
	SD.	120.3	2.0	9.9	0.4	5.7	56.2	8.5	0.1	108.8	50.4	46.0	58.8	2.0
	Var.	14479.5	4.0	97.8	0.2	32.2	3155.2	72.7	0.01	11827.4	2539.1	2114.6	3456.1	4.1
	CV	0.10	0.03	0.07	0.05	0.12	0.15	0.82	0.73	0.37	1.15	0.63	0.16	0.15

Notes: Min. = minimum; Max. = maximum; Mean = arithmetic mean; SD = standard deviation; Var. = variance; CV = coefficient of variation; N = number of geothermal water samples.
T denotes water temperature (°C); TDS denotes total dissolved solids. TDS, SiO_2, K^+, Na^+, Ca^{2+}, and Mg^{2+} are expressed in mg/L; pH is dimensionless.

4.2 Isotopes

Hydrogen and oxygen stable isotopes are important constituents of water molecules. Their abundances change during the hydrological cycle through evaporation, fractionation, and water mixing; their abundances and ratios can therefore be used to identify groundwater circulation processes and sources. As shown in Table 3, $\delta^{18}O$ values in Longmu Co geothermal water ranged from −13.44 to −15.01‰, and δD values ranged from −98.9 to −105.8‰. At Doma, $\delta^{18}O$ values ranged from −16.80 to −17.48‰, and δD values ranged from −140.5 to −143.6‰. At Yangbajing, $\delta^{18}O$ values ranged from −13.79 to −18.77‰, and δD values ranged from −141.0 to −149.9‰.

Table 3 Isotopic compositions of water samples and recharge elevations

Sample type	Sampling site	Sample ID	Sampling elevation	$\delta^{18}O$ V-SMOW	δD V-SMOW	$\delta^{13}C$ V-PDB	^{3}H	Recharge elevation
			m	(‰)	(‰)	(‰)	(TU)	(m)
Geothermal water	Longmu Co	BQT01	5090	-14.7	-104.3	1.36	3.82	5440
		BQT02	5094	-13.44	-98.9	4.20	3.24	5236
		BQT03	5089	-15.01	-105.8	1.13	3.43	5497
	Doma	NQT01	4683	-17.44	-142.9	2.64	＜2	6329
		NQT02	4684	-17.18	-141.8	3.27	＜2	6288
		NQT03	4685	-17.38	-142.8	3.02	＜2	6327
		NQT04	4686	-16.80	-140.5	4.21	＜2	6240
		NQT05	4688	-17.36	-142.8	3.25	＜2	6330
		NQT06	4689	-17.48	-143.6	2.58	＜2	6362
	Yangbajing	YBJ01	4288	-17.68	-148.2	-5.72	＜2	5358
		YBJ02	4289	-18.77	-150.2	-6.22	＜2	5436
		YBJ03	4290	-18.09	-149.8	-5.15	＜2	5422
		YBJ04	4291	-16.20	-145.1	-3.82	＜2	5242
		YBJ05	4292	-18.05	-149.9	-6.25	＜2	5428
		YBJ06	4293	-13.79	-141.0	-3.62	＜2	5086
Surface water	Longmu Co	LQ01	——	-13.24	-95.2	——	18.01	——
	Doma	LQ02	——	-13.05	-100.1	——	9.9	——
	Yangbajing	LQ03	——	-16.73	-120.37	——	——	——

Different carbon sources have markedly different $\delta^{13}C$ compositions, and $\delta^{13}C_{DIC}$ (the carbon isotopic composition of dissolved inorganic carbon) can provide key information on carbon sources and fluid evolution (Alçiçek et al. 2019). Among inorganic sources, atmospheric CO_2 has a $\delta^{13}C$ value of approximately −7‰, upper mantle carbon ranges from −8 to −4‰, and carbon derived from thermal decomposition or metamorphism of carbonate rocks ranges from −2 to +2‰; marine carbonate rocks typically have $\delta^{13}C$ values close to 0‰ or positive values. Organic carbon generally has more negative $\delta^{13}C$ values, ranging from −10 to −35‰, with characteristic biogenic values of approximately −22 to −25‰ (Foroutan et al. 2021; Hartanto et al. 2022). In geothermal water at Longmu Co in northern Qiangtang, $\delta^{13}C_{DIC}$ values ranged from 1.13 to 4.20‰, suggesting two possible sources: metamorphic decarbonation of carbonate rocks or dissolution of marine carbonate minerals. At Doma in southern Qiangtang, geothermal water had $\delta^{13}C_{DIC}$ values of 2.58–4.21‰, which, in combination with the regional geology, may reflect dissolution of marine carbonate rocks. At

Yangbajing, $\delta^{13}C_{DIC}$ values ranged from −3.62 to −6.25‰, within the range of upper mantle carbon. In the context of the regional tectonic setting, a contribution of mantle-derived CO_2 to the carbon component is possible, but further verification using other gas isotopic indicators is required.

Tritium (^3H) is a naturally occurring radioactive isotope of hydrogen with a half-life of approximately 12.32 years. Large-scale thermonuclear testing in the 1950s and 1960s caused a sharp increase in atmospheric ^3H concentrations, followed by a progressive decline. Accordingly, ^3H concentrations in geothermal water have been used to provide preliminary estimates of groundwater circulation rates and to identify mixing with modern water (Guo 2012). Concentrations below 1 TU indicate a predominance of old water that infiltrated before 1952, whereas concentrations above 1 TU indicate a signal of recharge or mixing with modern precipitation. At Longmu Co in northern Qiangtang, the ^3H concentration in surface water was 18.01 TU, whereas geothermal water concentrations ranged from 3.24 to 3.82 TU. These values, above 1 TU but below the local surface water concentration, indicate mixing between deep old water and shallow modern water. All geothermal water samples from Doma and Yangbajing had ^3H concentrations below the detection limit (<2 TU). This weak tritium signal indicates a very small contribution from modern precipitation and relatively long fluid residence times.

5 Discussion

5.1 Hydrochemical characteristics of geothermal water

The Schoeller diagram (Fig. 2) shows broadly similar cation patterns among the three groups of geothermal fluids, with Na^+ dominant and Mg^{2+} having the lowest concentration in milliequivalents. These characteristics indicate that all three groups have undergone water–rock interaction to varying degrees. Nevertheless, ionic concentrations differ markedly among the tectonic belts. The cation abundance sequence is $Na^+ > Ca^{2+} > K^+ > Mg^{2+}$ at both Longmu Co and Doma, whereas it is $Na^+ > K^+ > Ca^{2+} > Mg^{2+}$ at Yangbajing.

In contrast to the relatively convergent cation patterns, the anion compositions of the three geothermal systems show pronounced spatial differentiation on the Schoeller diagram. HCO_3^- dominates the anions in Doma geothermal water, which has relatively low Cl^- concentrations and an anion abundance sequence of $HCO_3^- > SO_4^{2-} > Cl^- > F^-$. At Yangbajing, the sequence is $Cl^- > HCO_3^- > SO_4^{2-} > F^-$; Cl^- is the dominant anion, SO_4^{2-} has the lowest concentration, and CO_3^{2-} was detected in some samples. The anion patterns of Longmu Co geothermal water are intermediate between those of Yangbajing and Doma. HCO_3^- and Cl^- concentrations are similar, and the anion abundance sequence is $Cl^- > HCO_3^- > SO_4^{2-} > F^-$.

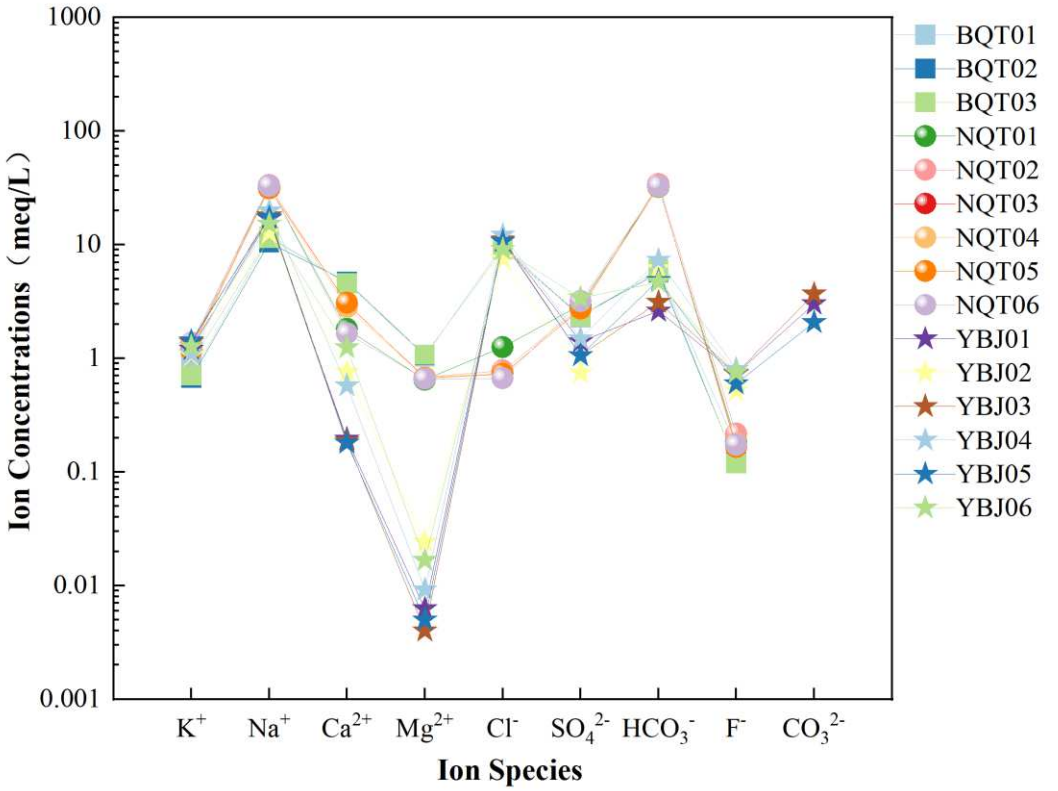


Fig. 2 Schoeller diagram

Piper diagrams provide a direct means of identifying hydrochemical types and evolutionary patterns of geothermal fluids in different tectonic units (Zheng et al. 2019). Projection of the geothermal water samples (Fig. 3) reveals distinct clusters for the three regions, reflecting differences in hydrochemical evolution pathways among the tectonic settings.

In the cation triangle on the left, all geothermal water samples cluster in the lower-right region near the ($Na^+ + K^+$) apex, indicating Na^+ (K^+)-dominated water. This distribution suggests that silicate mineral dissolution or cation exchange with the host rocks during deep circulation ultimately made Na^+ the dominant cation in all three systems. Despite this common pattern, subtle differences occur among the tectonic blocks: samples from Yangbajing and Doma lie closer to the rightmost ($Na^+ + K^+$) axis, whereas Longmu Co samples are shifted slightly toward the Ca^{2+} apex. Compositional differentiation is more pronounced in the anion triangle on the right. Doma samples cluster near the ($HCO_3^- + CO_3^{2-}$) apex and represent typical HCO_3–Na water. Most samples from Yangbajing and Longmu Co plot on the Cl^--enriched side, where Cl^- is the predominant anion. In the context of the regional geology, the chloride enrichment at Longmu Co may result from leaching of halite-bearing host-rock minerals, whereas Cl^- in Yangbajing geothermal fluids may partly reflect recharge by ascending, deep, chloride-rich thermal fluids. According to the Shchukarev classification (Table 4), the hydrochemical types are $Cl \cdot HCO_3$–Na·Ca at Longmu Co in northern Qiangtang, HCO_3–Na at Doma in southern Qiangtang, and $Cl \cdot HCO_3$–Na at Yangbajing.

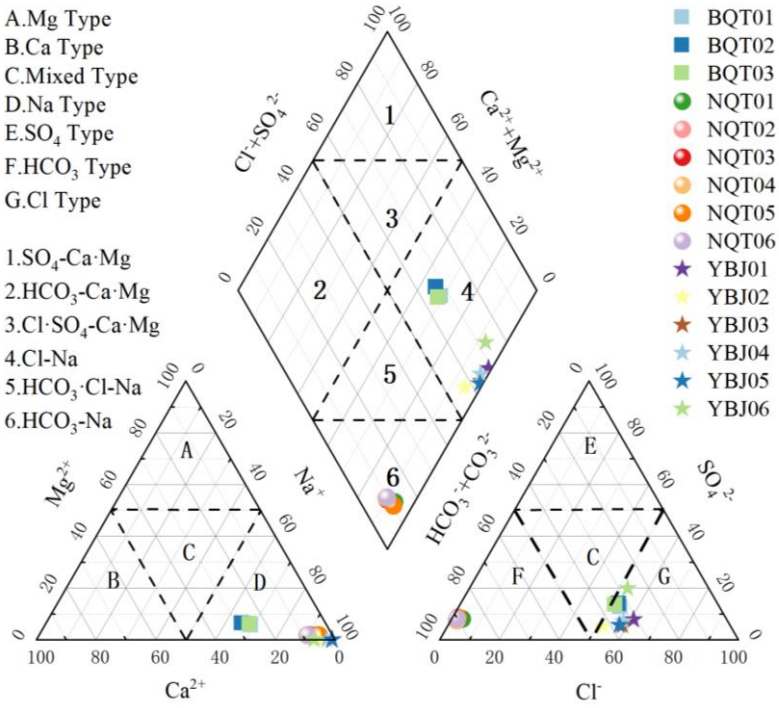


Fig. 3 Piper diagram of water samples

Table 4 Hydrochemical types of geothermal water

Sample ID	Sampling site	Hydrochemical type	Equivalent concentration percentage (%)					
			K^++Na^+	Ca^{2+}	Mg^{2+}	HCO_3^-+CO_3^{2-}	Cl^-	SO_4^{2-}
BQT01	Longmu Co	Cl·HCO_3–Na·Ca	69.01	25.33	5.66	33.23	54.24	12.53
BQT02		Cl·HCO_3–Na·Ca	65.65	28.03	6.32	33.06	53.05	13.89
BQT03		Cl·HCO_3–Na·Ca	68.35	25.63	6.02	34.47	52.03	13.50
NQT01	Doma	HCO_3–Na	93.24	4.98	1.78	88.49	3.45	8.06
NQT02		HCO_3–Na	90.38	7.84	1.78	90.49	2.06	7.45
NQT03		HCO_3–Na	90.28	7.83	1.89	90.45	2.05	7.50
NQT04		HCO_3–Na	89.65	8.51	1.84	90.45	2.01	7.54
NQT05		HCO_3–Na	93.67	4.53	1.80	89.54	1.81	8.65
NQT06		HCO_3–Na	89.87	8.32	1.81	90.09	1.72	8.19
YBJ01	Yangbajing	Cl·HCO_3–Na	98.91	1.06	0.03	31.23	60.99	7.78
YBJ02		Cl·HCO_3–Na	94.63	5.21	0.17	42.77	52.05	5.18
YBJ03		Cl·HCO_3–Na	99.02	0.96	0.02	36.01	58.39	5.60
YBJ04		Cl·HCO_3–Na	97.29	2.67	0.04	34.99	57.90	7.11
YBJ05		Cl·HCO_3–Na	99.02	0.95	0.03	37.01	57.32	5.67
YBJ06		Cl·HCO_3–Na	92.92	6.99	0.09	27.20	53.03	19.77

Note: Hydrochemical types were determined using the Shchukarev classification, in which ions accounting for more than 25% of the equivalent concentration are included in the water-type designation.

Gibbs diagrams were originally developed to distinguish the processes controlling surface water composition. By integrating the Gibbs model with diagnostic ion ratios and hydrogen and oxygen isotope tracers (Chen et al. 2023), researchers have extended its application to the systematic identification of geothermal water formation mechanisms.

The Gibbs diagrams for geothermal water from Longmu Co, Doma, and Yangbajing (Fig. 4) show that TDS concentrations in all samples fall between 1000 and 3000 mg/L, indicating moderately to highly mineralized geothermal fluids. At Yangbajing and Longmu Co, $Cl^-/(Cl^- + HCO_3^-)$ ratios are concentrated between 0.5 and 0.9, and $Na^+/(Na^+ + Ca^{2+})$ ratios exceed 0.7. These samples plot in the upper-right evaporation–concentration field in both the anion and cation diagrams. Considering the occurrence of these geothermal fluids, this distribution does not result from evaporation and concentration in a near-surface environment. Instead, it reflects prolonged deep circulation accompanied by intense water–rock interaction at high temperatures, or mixing with deep, saline reservoir fluids enriched in Na^+ and Cl^-, ultimately producing ionic enrichment. At Doma, $Na^+/(Na^+ + Ca^{2+})$ ratios approach 1, whereas $Cl^-/(Cl^- + HCO_3^-)$ ratios approach 0. This pattern demonstrates the overwhelming dominance of HCO_3^- among the anions and indicates the influence of carbonate host-rock leaching or the input of deep CO_2 during fluid migration through the reservoir. In geothermal systems, Gibbs diagrams serve only as qualitative indicators because deep water–rock interaction and fluid mixing can also shift samples into the evaporation–concentration field. Interpretation therefore requires joint consideration of isotopic evidence and ion ratios.

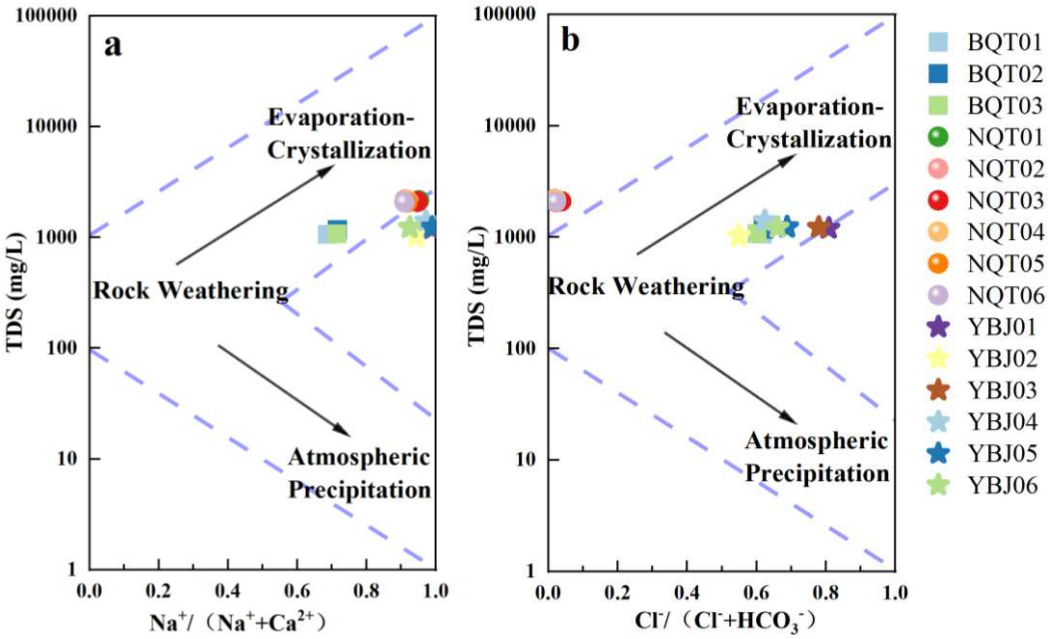


Fig. 4 Gibbs diagrams for hydrochemical analysis of geothermal water

Concentration ratios of major ions in geothermal water can indicate the mechanisms of water–rock interaction during deep circulation and provide key geochemical evidence for geothermal fluid formation and evolution (Zhou et al. 2023). These relationships are compared below to further identify the sources of the major ions.

The Ca^{2+}–SO_4^{2-} relationship in Fig. 5a shows that Longmu Co geothermal water is enriched in Ca^{2+} relative to SO_4^{2-}. This indicates that gypsum dissolution is not the principal source of these two ions and that an additional Ca^{2+} source is present. In combination with Fig. 5b and e, these results suggest that Ca^{2+} at Longmu Co is derived

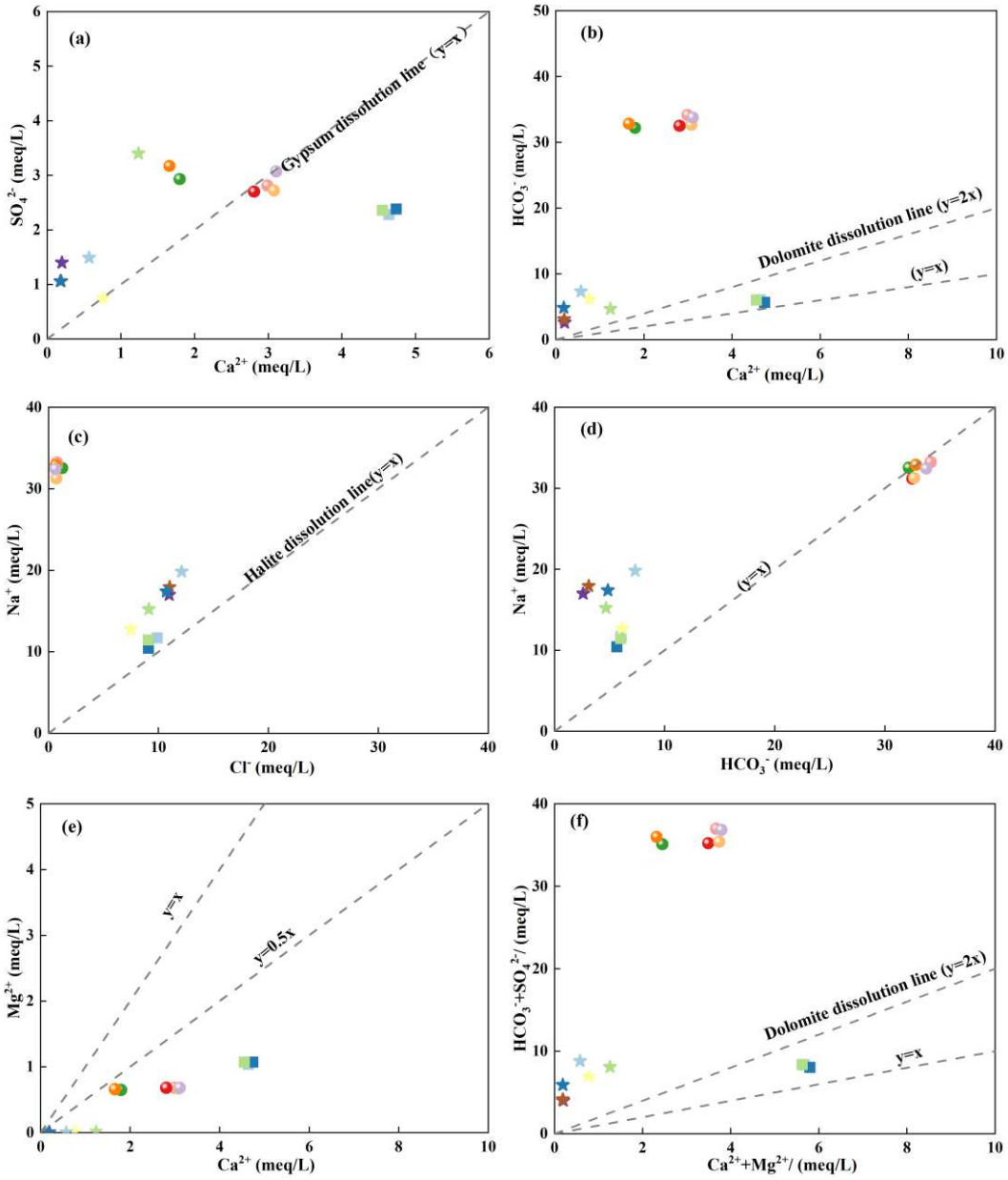
mainly from carbonate rock leaching. Doma samples plot mainly near the y = x line in the Ca^{2+}–SO_4^{2-} diagram, indicating that gypsum dissolution may supply an important proportion of the Ca^{2+} and SO_4^{2-}. However, reverse cation exchange causes substantial adsorption of Ca^{2+} onto the host rocks, maintaining low Ca^{2+} concentrations in the water. Most Yangbajing samples plot above the gypsum dissolution line and show a clear Ca^{2+} deficit relative to SO_4^{2-}. Together with the calcite saturation indices, this pattern suggests that cation exchange may consume some Ca^{2+} or that precipitation of minerals such as calcite removes Ca^{2+} from the water, resulting in relative SO_4^{2-} enrichment in the fluid.

When Na^+ and Cl^- are derived primarily from halite dissolution, their equivalent concentration ratio approaches 1. Figure 5c shows that Na^+/Cl^- ratios in Longmu Co geothermal water are close to 1, indicating a strong common-source relationship and suggesting that halite leaching may be their principal source. Na^+ concentrations in Doma geothermal water generally far exceed Cl^- concentrations. Considered together with the chloro-alkaline indices discussed below, this excess may result from cation exchange during geothermal water migration or from additional Na^+ supplied by silicate mineral dissolution. Yangbajing samples plot above the 1:1 line, indicating that halite leaching is the dominant process controlling the concurrent increase in Na^+ and Cl^-, with an additional Na^+ input beyond the equivalent amounts of Na^+ and Cl^- supplied by halite. The Na^+/HCO_3^- ratio is an important indicator of silicate dissolution. If both ions originate solely from albite dissolution in the host rocks, their ratio should theoretically approach 1. Longmu Co samples plot above the albite dissolution line (Fig. 5d), which, together with the preceding results, indicates that sodium is derived mainly from halite dissolution. Doma samples lie along the 1:1 line, indicating that hydrolysis of silicate minerals such as albite is an important Na^+ source. Feldspar hydrolysis releases Na^+, whereas deep CO_2 input and carbonate leaching supply abundant HCO_3^-; cation exchange provides an additional contribution of Na^+. At Yangbajing, Na^+/HCO_3^- ratios exceed 1, indicating an additional sodium source alongside silicate weathering during geothermal water formation and evolution.

The ratio between $(Ca^{2+} + Mg^{2+})$ and $(HCO_3^- + SO_4^{2-})$ can be used to identify the contributions of carbonate rock and some evaporite leaching to geothermal water chemistry. When these ions are derived entirely from calcite, dolomite, and gypsum dissolution, the $(HCO_3^- + SO_4^{2-})/(Ca^{2+} + Mg^{2+})$ ratio approaches 1. In Fig. 5f, samples from Doma and Yangbajing generally plot above the 1:1 line, indicating contributions of HCO_3^- and SO_4^{2-} from sources other than carbonate rocks and evaporites, potentially including deep volatile CO_2 or shallow mineral dissolution (Zhang et al. 2021). In particular, the pronounced HCO_3^- excess in Doma geothermal water suggests that substantial deep CO_2 may have entered the system. Under these conditions, silicate weathering, such as albite and K-feldspar hydrolysis, supplies abundant Na^+ to maintain cation–anion balance (Fisher and Mullican 1997).

The chloro-alkaline indices CAI-1 and CAI-2 are key indicators of the direction and intensity of cation exchange between groundwater and its host rocks. Negative values indicate forward cation exchange, in which Ca^{2+} and Mg^{2+} in the water displace

Na^+ and K^+ from the host rocks, resulting in pronounced Na^+ enrichment in the water; positive values indicate reverse exchange. The relationship between ($Ca^{2+} + Mg^{2+} - SO_4^{2-} - HCO_3^-$) and ($Na^+ + K^+ - Cl^-$), together with the distance of each data point from the origin, can also be used to infer the intensity of cation exchange during geothermal water circulation and migration. As shown in Fig. 5g and h, the chloro-alkaline indices of all spring water samples from Longmu Co, Doma, and Yangbajing are negative, and the data points cluster closely around the ion-exchange line.



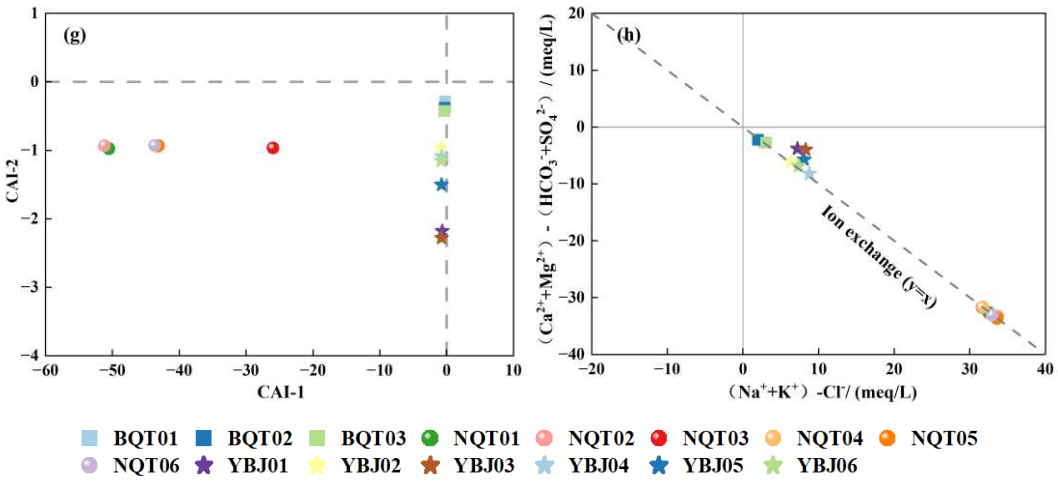


Fig. 5 Hydrochemical ion-ratio diagrams

This indicates that geothermal waters in all three regions experienced forward cation exchange during deep circulation and flow, although the characteristics differ markedly among regions. In Fig. 5h, Longmu Co samples lie close to the origin, reflecting relatively weak exchange. Doma samples lie far from the origin, reflecting intense cation exchange during geothermal water circulation that produced distinctly Na-rich water. This confirms a deep reservoir environment characterized by strong confinement, long circulation pathways, and slow circulation. Yangbajing data points show some displacement along the 1:−1 line, indicating weaker cation exchange than at Doma.

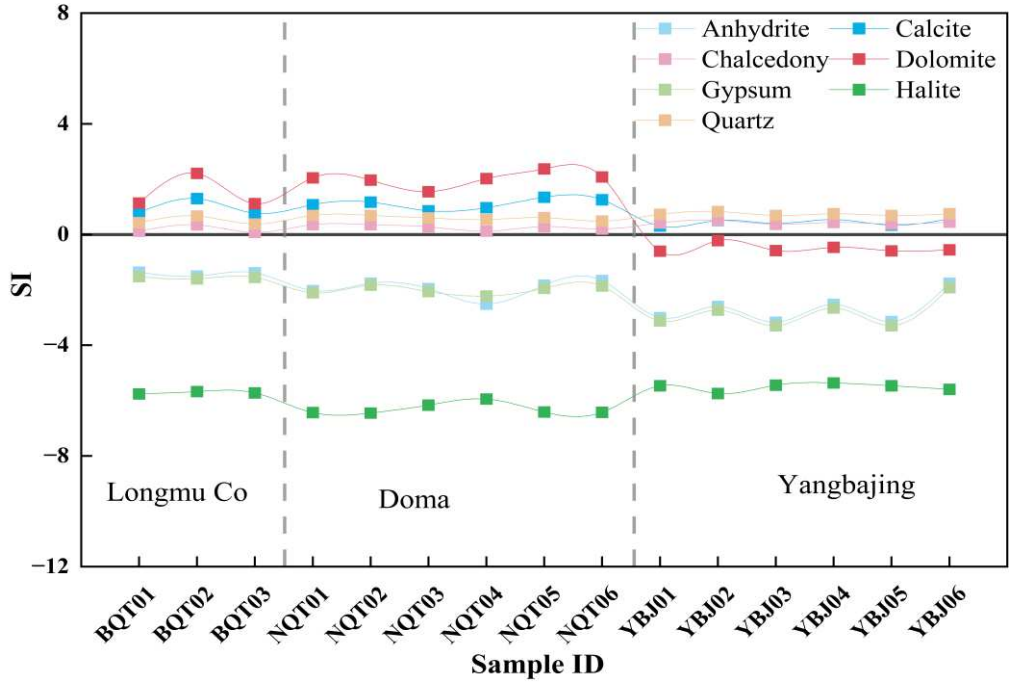


Fig. 6 Saturation indices (SI) of selected minerals in the studied waters

Figure 6 shows the saturation indices of major minerals in geothermal waters from Longmu Co, Doma, and Yangbajing. Calcite, quartz, and chalcedony are supersaturated in all three systems, indicating a thermodynamic tendency toward mineral precipitation.

Anhydrite, gypsum, and halite are undersaturated, indicating the potential for further leaching if these minerals are present in the host rocks. Dolomite is also supersaturated in geothermal waters from Doma and Longmu Co. Although the dolomite saturation indices at Yangbajing are below 0, they approach saturation.

5.2 Recharge sources and elevations of geothermal water

Hydrogen and oxygen isotopes are natural tracers of water molecules that help characterize fluid origins, recharge mechanisms, and deep evolution. They provide strong evidence for interpreting geothermal system genesis and the intensity of water–rock interaction. Comparing the isotopic compositions of geothermal waters with the global and local meteoric water lines (GMWL and LMWL), magmatic water, and snow and ice meltwater can identify recharge sources (Craig 1961; Giggenbach 1992; Guo et al. 2010). The isotopic elevation effect can also be used to estimate recharge elevations. Figure 7 shows the δD–$\delta^{18}O$ relationships for the three groups of geothermal waters. All three groups plot near the meteoric water lines, indicating that meteoric water is their principal recharge source. At Longmu Co, both surface water and geothermal water plot close to the meteoric water lines, indicating direct meteoric recharge. Despite the substantial circulation depths of the geothermal fluids, isotopic exchange with the surrounding rocks is weak, and the original recharge-water signatures are largely preserved. At Doma, geothermal water and surface water occupy distinctly different positions in the hydrogen–oxygen isotope diagram. Although the geothermal waters plot near the mixing trend between snow and ice meltwater and magmatic water, they remain far from the magmatic endmember. The contribution of magmatic water is therefore limited. Recharge is dominated by meteoric water and snow and ice meltwater, with a potential signal of magmatic-water mixing. However, this isotopic pattern is more likely to reflect an oxygen shift caused by deep water–rock isotopic exchange. Doma geothermal waters have markedly more negative δD and $\delta^{18}O$ values than local surface water. The depleted δD values indicate recharge from high-elevation water sources (Pichler 2005). At Yangbajing, geothermal waters are markedly depleted in δD relative to surface water, indicating recharge from high-elevation precipitation or snow and ice meltwater. Their distribution along the snow and ice meltwater–magmatic water trend suggests water–rock isotopic exchange or the potential mixing of minor magmatic fluids.

Equation 1 was used to estimate the elevations and extent of the recharge areas. A δD elevation gradient of −2.6 ‰/100 m for southwestern China was adopted (D'Amore and Panichi 1985). This gradient is an empirical regional parameter, so the calculated recharge elevations are estimates subject to uncertainty. The results indicate recharge elevations of 5236–5497 m for Longmu Co geothermal water (Table 3). Local topographic elevations and the hydrogen–oxygen isotope results discussed above suggest that recharge occurs in the mountainous area to the east. Estimated recharge elevations for Doma geothermal water range from 6240 to 6362 m, exceeding the highest elevations near the study area. This suggests that recharge is not derived directly from present-day local precipitation. Instead, it may originate from precipitation in distant high-elevation mountains or from paleoprecipitation during colder periods.

Estimated recharge elevations for Yangbajing geothermal water range from 5086 to 5436 m. Considering the surrounding topography and regional geological and geomorphological setting, the snowline in the Nyainqentanglha Mountains near the springs lies at 5500 m (Tan et al. 2014). This closely matches the estimated recharge-elevation range, indicating that high-elevation precipitation and snow and ice meltwater are the principal recharge sources.

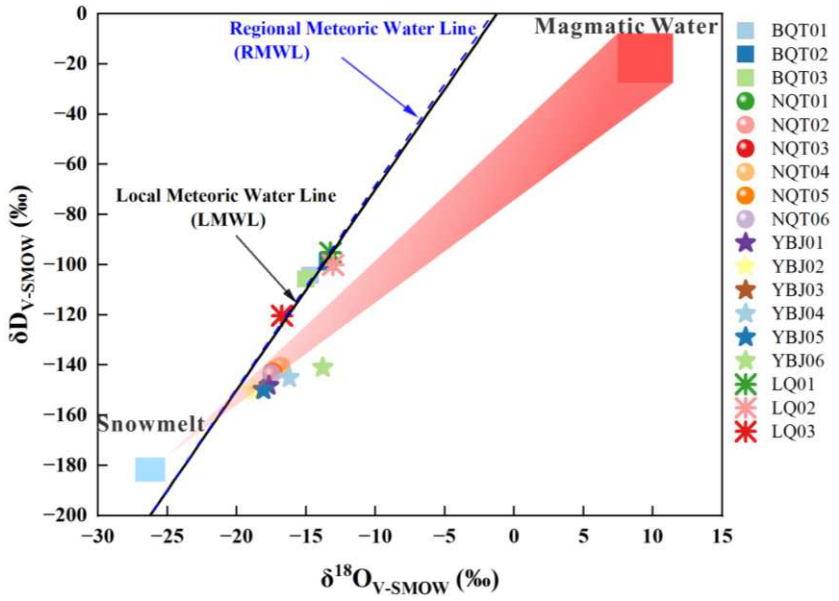


Fig. 7 δD–δ^{18}O relationships of the water samples (δD–δ^{18}O scatter plot)

5.3 Reservoir temperature

Cation geothermometers are widely used geothermal tracers based on quantitative relationships between cation partition coefficients and temperature during water–rock equilibrium reactions. Their predictions depend on empirical calibration and are therefore semi-empirical quantitative estimates (Giggenbach 1988). Giggenbach combined the Na–K and K–Mg geothermometers to develop the Na–K–Mg ternary diagram (Fournier and Potter 1979). This diagram uses quantitative relationships between ionic concentration ratios and temperature to distinguish fully equilibrated, partially equilibrated, and immature waters. It assesses water–rock equilibrium and the reliability of cation geothermometer estimates. In Fig. 8, Yangbajing geothermal waters plot in the partial-equilibrium field, whereas the Longmu Co and Doma samples fall in the immature-water field. These distributions indicate incomplete water–rock interaction or mixing with shallow cold water during ascent. Reservoir temperatures calculated using different cation geothermometers vary considerably. The Na–K geothermometer yields 221–244 °C for Longmu Co, 178–188 °C for Doma, and 212–249 °C for Yangbajing. The corresponding K–Mg estimates are 88–97 °C, 109–114 °C, and 160–208 °C, respectively. Cation geothermometers are based on thermodynamic equilibrium, whereas none of the sampled geothermal waters has attained equilibrium. Their reservoir temperature estimates may therefore be substantially biased and are presented for reference only.

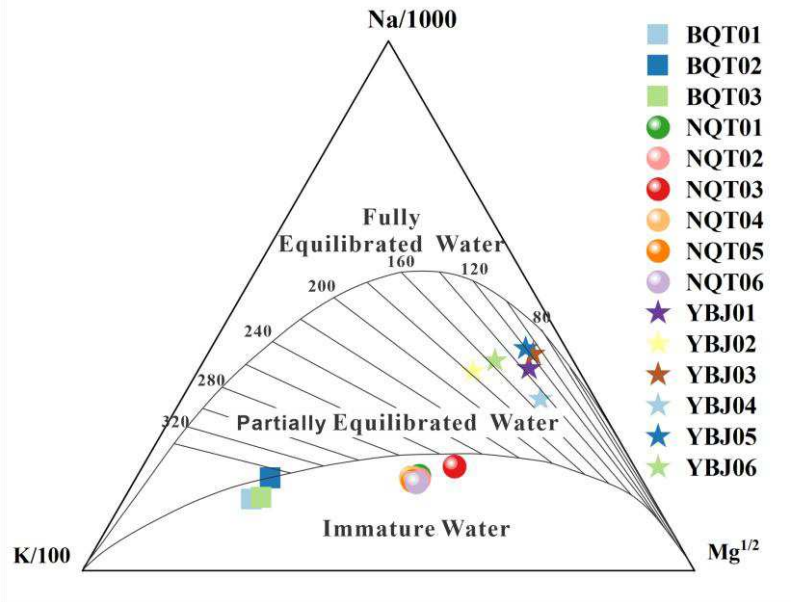


Fig. 8 Na–K–$Mg^{1/2}$ ternary diagram of geothermal waters

Silica geothermometry is a principal tool for estimating deep reservoir temperatures (Guo et al. 2020; Zheng et al. 2015). Because silica mineral phases, including quartz and chalcedony, differ in their solubility controls, their temperature responses must be evaluated systematically to identify the most appropriate geothermometer. The lg(SiO_2)–lg(K^2/Mg) diagram (Fig. 9) was used to assess the dissolution states of silica minerals and their suitability for geothermometry. The sample distributions indicate differences in silica-controlling mineral phases and fluid evolution among the geothermal systems. Doma and Longmu Co waters generally plot between the quartz and chalcedony curves, indicating silica concentrations between their respective equilibrium solubilities. Quartz is interpreted as the mineral controlling silica equilibrium in these reservoirs. Most Yangbajing samples plot below the quartz reference curve, possibly reflecting physical mixing with shallow, low-silica cold water during ascent along faults.

The calculated results are presented in Table 5. The quartz geothermometer without steam loss yields 111–138 °C for Longmu Co, 126–134 °C for Doma, and 153–164 °C for Yangbajing. The quartz geothermometer with maximum steam loss yields 110–133 °C, 123–130 °C, and 146–155 °C, respectively. The chalcedony geothermometer without steam loss yields 81–111 °C for Longmu Co, 98–107 °C for Doma, and 128–141 °C for Yangbajing. The corresponding estimates with maximum steam loss are 82–110 °C, 98–105 °C, and 125–137 °C, respectively. Silica geothermometry applied directly to the SiO_2 concentrations of collected samples underestimates the original deep reservoir temperatures. A silica–enthalpy mixing model is therefore required to account for cold-water mixing and reconstruct deep reservoir conditions before mixing.

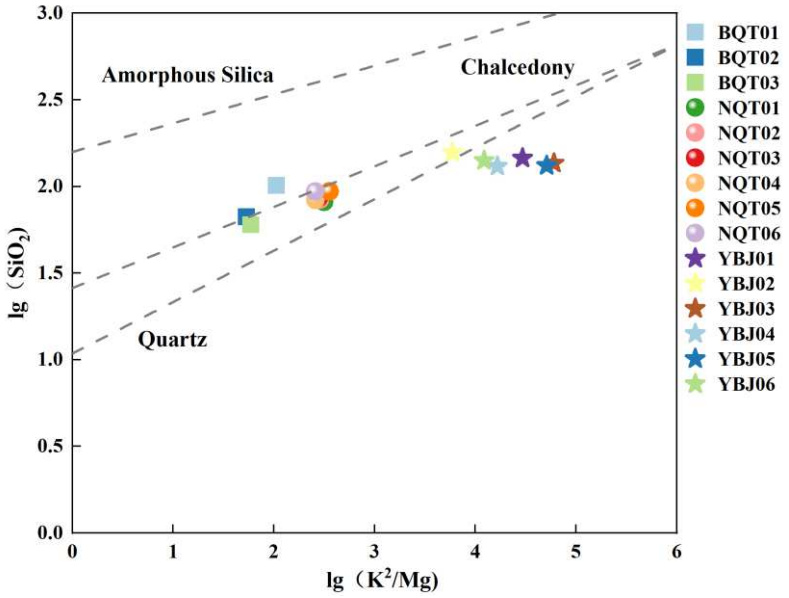
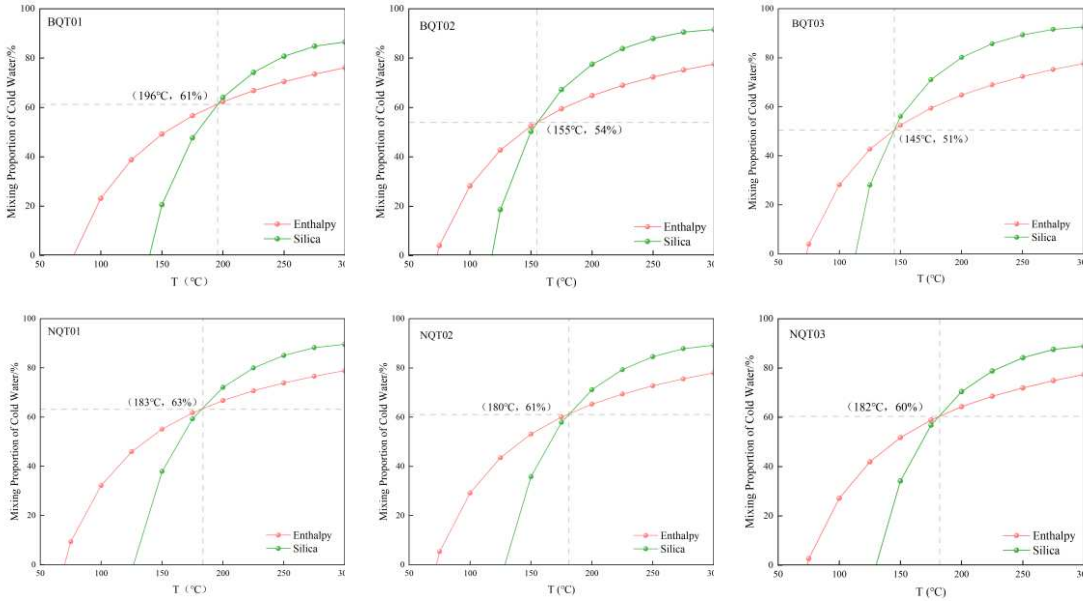


Fig. 9 Distribution of silica (SiO_2) in the geothermal waters

Conventional cation and silica geothermometers are susceptible to cold-water mixing, which can introduce substantial bias into their temperature estimates. A silica–enthalpy mixing model was therefore applied to estimate deep reservoir temperatures before mixing and the cold-water mixing fractions. For each spring system, the local surface cold water considered to be closely hydraulically connected to the springs was selected as the cold endmember. This selection was intended to represent the local mixing process. The results are shown in Fig. 10. The silica–enthalpy equations yield reservoir temperatures of 145–196 °C and cold-water mixing fractions of 51–61% for Longmu Co, indicating medium- to high-temperature geothermal resources. For Doma, the estimated reservoir temperatures are 175–192 °C and the cold-water mixing fractions are 57–63%, indicating high-temperature geothermal resources. Yangbajing has estimated reservoir temperatures of 225–247 °C and cold-water mixing fractions of 66–69%, also indicating high-temperature geothermal resources.



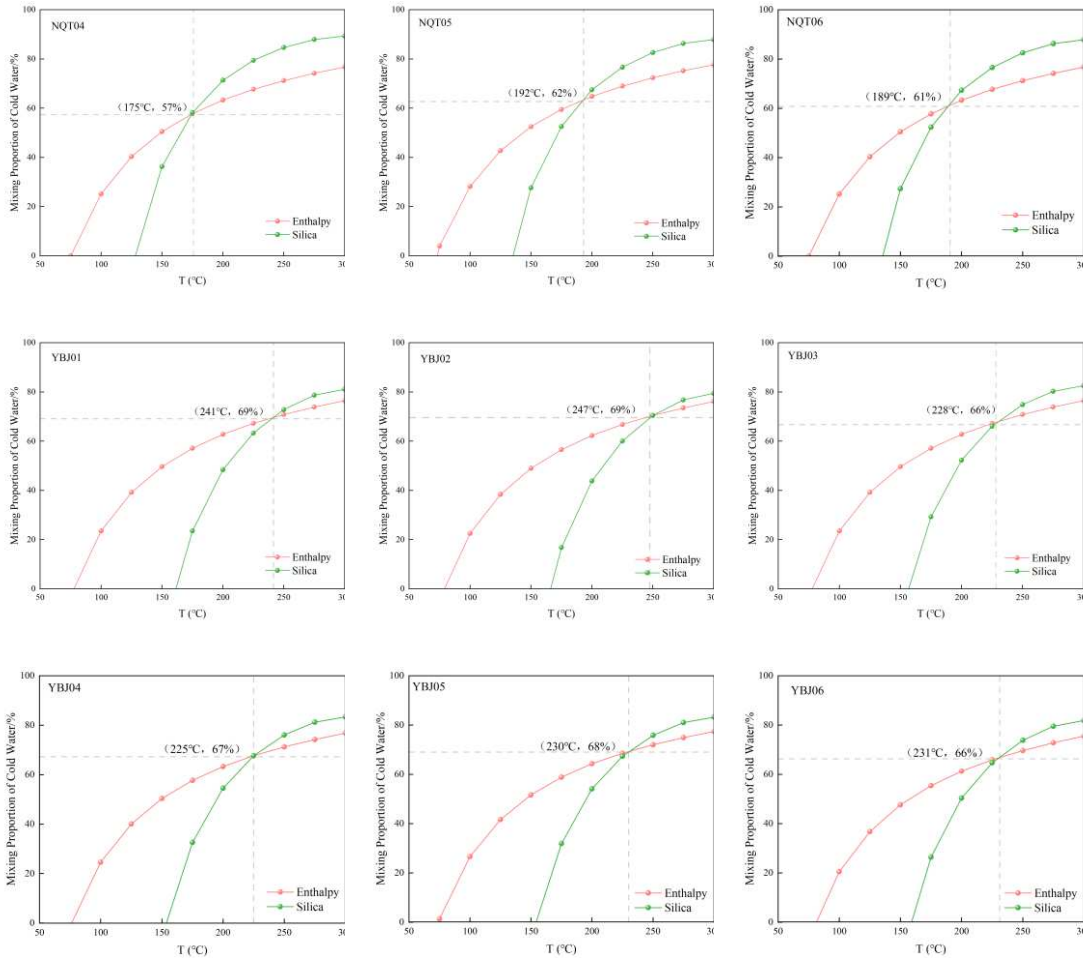


Fig. 10 Geothermal water sample diagrams based on the silica–enthalpy equations

5.4 Geothermal water circulation depth

The estimated reservoir temperatures differ considerably because the methods rely on different theoretical principles, applicability conditions, and assumptions about subsurface physicochemical processes. Cation geothermometers apply only to geothermal fluids in full water–rock equilibrium. Silica geothermometers applied directly to mixed water samples cannot account for dilution by cold water. The geothermal waters in the study areas contain substantial proportions of mixed cold water. Because the silica–enthalpy mixing model accounts for this mixing effect, its estimates of original reservoir temperatures are more appropriate for estimating deep reservoir temperatures and circulation depths.

Based on previous studies, the depth of the constant-temperature zone was set to 30 m (Fournier 1977). The mean annual air temperatures were set to 0.5 °C for Qiangtang and 2.5 °C for Yangbajing (Ma 2021; Zheng et al. 2019). Geothermal gradients of 29 °C/km, 26.5 °C/km, and 46 °C/km were adopted for Longmu Co, Doma, and Yangbajing, respectively (Liu et al. 2026; Ren et al. 2015; Ye and Mao 2024). These parameters were substituted into the circulation-depth equation, yielding the results in Table 5. Estimated circulation depths are 5047–6806 m for Longmu Co, 6653–7294 m for Doma, and 4867–5345 m for Yangbajing. The estimated circulation depth of

Longmu Co sample BQT01 is markedly greater than those of the other two samples. This suggests that its fluid may originate from a deeper reservoir and indicates a multilayer reservoir structure at Longmu Co. Doma has the greatest circulation depths, indicating deep fluid percolation and circulation along regional deep-seated major faults. Yangbajing fluids circulate at comparatively shallower depths, yet their reservoir temperatures are markedly higher than those in Qiangtang. This indicates a locally anomalous geothermal gradient, with deep heat sources closely associated with residual heat from young, localized magmatism in the southern Tibetan Plateau.

Table 5 Reservoir temperatures and circulation depths estimated using different methods

Sample ID	Na–K (°C)	K–Mg (°C)	Quartz, no steam loss (°C)	Quartz, maximum steam loss (°C)	Chalcedony, no steam loss (°C)	Chalcedony, maximum steam loss (°C)	Silica–enthalpy model (°C)	Cold-water mixing fraction (%)	Circulation depth (m)
BQT01	244	97	138	133	111	110	196	61	6806
BQT02	225	88	116	115	87	87	155	54	5392
BQT03	221	89	111	110	81	82	145	51	5047
NQT01	184	112	126	123	98	98	183	63	6955
NQT02	181	111	128	125	100	99	180	61	6841
NQT03	184	110	129	126	101	101	182	60	6917
NQT04	181	109	127	124	100	99	175	57	6653
NQT05	188	114	134	130	107	105	192	62	7294
NQT06	178	109	133	130	106	105	189	61	7181
YBJ01	233	192	159	151	135	132	241	69	5215
YBJ02	249	160	164	155	141	137	247	69	5345
YBJ03	241	208	155	148	131	128	225	67	4867
YBJ04	212	180	153	146	128	125	228	66	4932
YBJ05	247	204	153	146	128	125	230	68	4976
YBJ06	249	174	157	150	133	130	231	66	4997

5.5 Conceptual model of geothermal system genesis

Comparison of the Longmu Co, Doma, and Yangbajing geothermal systems in northern Qiangtang, southern Qiangtang, and the Lhasa terrane reveals shared and contrasting formation mechanisms. These patterns characterize geothermal systems in different tectonic settings across the central and southern Tibetan Plateau.

The Longmu Co geothermal system in northern Qiangtang lies near the Longmu Co–Shuanghu suture zone and contains a well-developed fault system. Its geothermal waters are of the Cl·HCO_3–Na·Ca type. Their chemistry reflects the combined effects of carbonate and evaporite dissolution and shallow evaporation–crystallization, indicating complex water–rock interaction. Estimated reservoir temperatures range from 145 to 196 °C, with circulation depths of 5047–6806 m. The considerable differences among samples indicate a multilayer reservoir structure, with waters potentially originating from reservoirs at different depths. Moho offsets and intracrustal melt bodies occur beneath Qiangtang. The geothermal heat supply is attributed to a combination of localized intracrustal melting and mantle heat flow. Glacier meltwater and precipitation from the mountains surrounding the sampling sites provide geothermal recharge, infiltrating downward and being stored in the reservoirs. During

deep circulation, the water undergoes intense interaction with the surrounding rocks. After absorbing sufficient heat and attaining thermal equilibrium within the reservoirs, groundwater rises along preferential fault and fracture pathways. Hydraulic head from high elevations and deep thermal buoyancy jointly drive this ascent, producing hot springs at the surface. The ascending fluids mix with a proportion of shallow cold water.

The Doma geothermal system in southern Qiangtang lies near the Bangong Co–Nujiang suture zone. Nearly east–west-trending major faults and subsidiary conjugate strike-slip fracture networks are widespread, providing effective pathways for fluid flow and heat transport. The geothermal water chemistry is jointly controlled by silicate and evaporite dissolution and cation exchange. Estimated reservoir temperatures of 175–192 °C and circulation depths of 6653–7294 m characterize a typical deep-circulation geothermal system. Recharge elevations are estimated at 6240–6362 m, with recharge dominated by distant high-elevation precipitation and snow and ice meltwater. Strong compression of crustal and mantle materials during plate collision generated abundant deep crustal melts. The geothermal heat sources therefore mainly comprise deep mantle heat flow and localized shallow melt bodies. Water infiltrating from high-elevation recharge areas circulates over long distances at depth and gains heat from the regional geothermal gradient. Volatile components, including CO_2 released along deep faults, enter the groundwater and promote carbonate and silicate mineral dissolution under high-temperature, high-pressure conditions. Combined with intense cation exchange, these processes enrich the geothermal fluids in Na^+, HCO_3^-, SiO_2, and other components, producing the characteristic HCO_3–Na waters. Driven by temperature and pressure, geothermal fluids rise along permeable pathways and discharge as hot springs, mixing with shallow cold water during ascent.

Following prolonged compression and crustal thickening, the Lhasa terrane developed an extensive system of nearly north–south-trending extensional rifts. The Damxung–Yangbajing fault zone occupies the core of this regional strike-slip and extensional tectonic system. Intense deformation disrupted the continuity of the strata, creating a fault network that provides effective pathways for hydrothermal circulation. The geothermal waters are of the Cl·HCO_3–Na type, with chemistry influenced jointly by water–rock interaction and cation exchange. Estimated reservoir temperatures range from 225 to 247 °C, with circulation depths of 4867–5345 m. The principal heat sources are incompletely cooled, young granitic magma chambers formed by plate movement in the shallow crust, together with deep mantle heat flow. Precipitation and snow and ice meltwater from the Nyainqentanglha Mountains provide the main recharge. Driven by gravitational head, this water infiltrates and undergoes deep convective circulation along extensional faults. As fluids pass through magma chambers and high-temperature source regions, they absorb substantial heat and receive deep magmatic volatile components. This produces high-temperature hydrothermal fluids driven by a mixed crustal and mantle heat supply. High temperatures promote intense dissolution of basement rocks and extensive water–rock interaction. Density differences between hot and cold fluids drive upward flow through the fracture network. Substantial shallow cold-water mixing then occurs before the fluids discharge as hot springs.

The geothermal systems display clear tectonic differentiation and shared hydrothermal evolutionary characteristics from north to south across the Tibetan Plateau. All three systems are mainly recharged by high-elevation precipitation and snow and ice meltwater. Fluids circulate deeply along fault systems and gain heat from the regional deep thermal regime or localized intracrustal thermal anomalies. Mixing with shallow cold water accompanies ascent and surface discharge in all three systems. However, tectonic setting controls differences in their genetic types. Longmu Co is a medium- to high-temperature geothermal system controlled by tectonic and magmatic activity (Wang et al. 2019; Xu et al. 2020). Doma is a structurally controlled, deep-circulation, high-temperature geothermal system. Yangbajing is a convective high-temperature geothermal system with a magmatic heat source (Duo 2003).

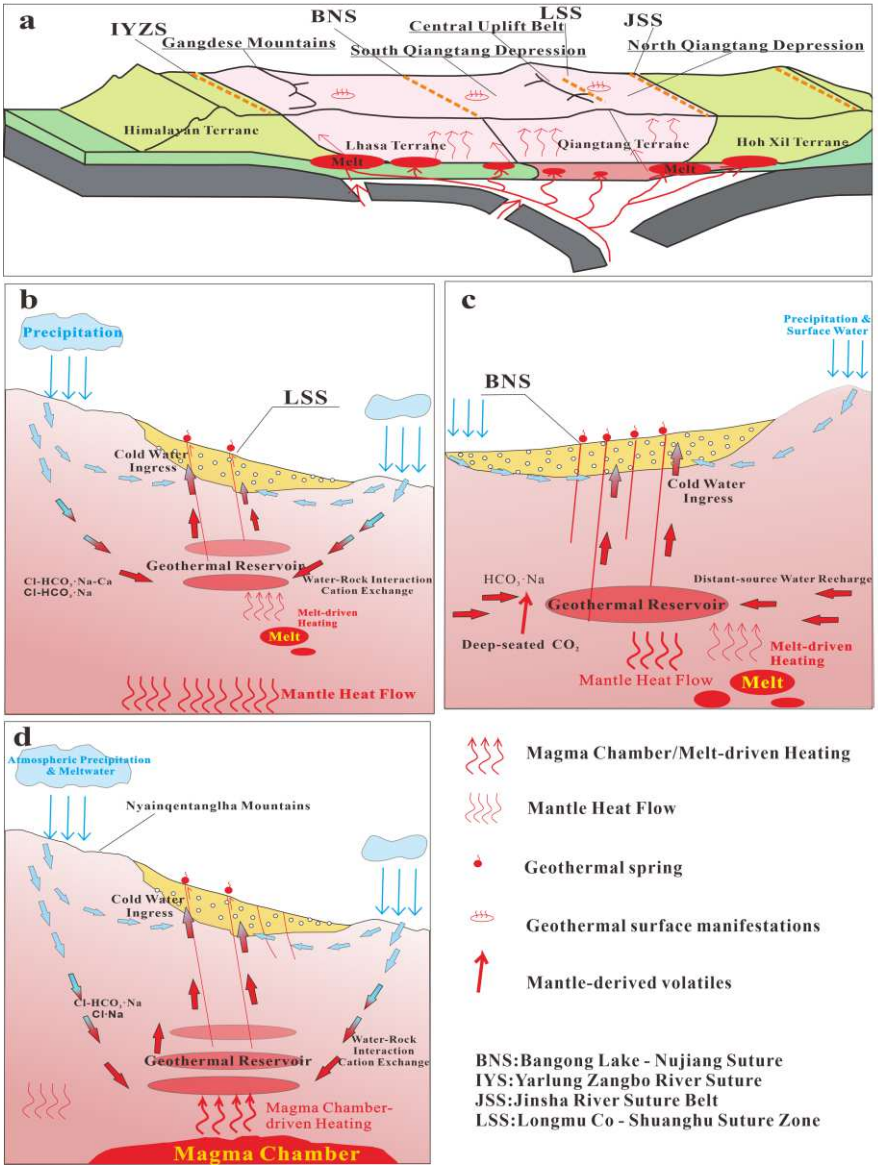


Fig. 11 Genetic models of the geothermal systems. (a) Regional geothermal genetic model (Ding et al. 2022; Shi et al. 2024); (b) schematic circulation model for Longmu Co geothermal water in

northern Qiangtang; (c) circulation model for Doma geothermal water in southern Qiangtang; (d) circulation model for Yangbajing geothermal water in the Lhasa terrane

6 Conclusions

Yangbajing in the Lhasa terrane and Doma and Longmu Co in the Qiangtang terrane occupy three different tectonic units. Their geothermal systems differ in hydrochemical type, recharge source, reservoir temperature, and reservoir type, as summarized below.

1. Longmu Co geothermal waters are of the $Cl{\cdot}HCO_3$–$Na{\cdot}Ca$ type, Doma waters are of the HCO_3–Na type, and Yangbajing waters are predominantly of the $Cl{\cdot}HCO_3$–Na type. These hydrochemical types are controlled by reservoir depth, the intensity of water–rock interaction, and cold-water mixing during fluid ascent.

2. Longmu Co geothermal water is recharged by precipitation and snow and ice meltwater from the mountainous area east of the study area. Estimated recharge elevations are 5236–5497 m, with circulation depths of 5047–6806 m. Doma geothermal water is recharged by precipitation and snow and ice meltwater from distant high-elevation mountains. Gaseous components, including CO_2 released from deep intracrustal melts, contribute to regulating the fluid chemistry. Estimated recharge elevations are 6240–6362 m, with circulation depths of 6653–7294 m. Yangbajing geothermal water has estimated recharge elevations of 5086–5436 m and circulation depths of 4867–5345 m. It originates from precipitation and snow and ice meltwater in the nearby Nyainqentanglha Mountains and receives deep volatile components released from magma chambers.

3. Among the three systems, reservoir temperatures are highest at Yangbajing in the south, followed by Doma in the central area, whereas Longmu Co in the north spans a broader range. Southernmost Yangbajing has reservoir temperatures of 225–247 °C and is classified as a high-temperature geothermal system. Doma has the next-highest temperatures, ranging from 175 to 192 °C, and is also classified as a high-temperature geothermal system. Longmu Co has a broader reservoir temperature range of 145–196 °C, suggesting that fluids may originate from reservoirs at different depths. Its samples span the medium- to high-temperature range.

4. The silica–enthalpy mixing model indicates varying degrees of cold-water mixing during fluid ascent in all three systems. Estimated cold-water mixing fractions are 51–61% at Longmu Co, 57–63% at Doma, and 66–69% at Yangbajing. Substantial cold-water mixing lowers geothermal water temperatures at the spring outlets.

5. Yangbajing lies near the Gangdese belt of the Lhasa terrane. Shallow intracrustal melt bodies form magma chambers that provide the principal sustained heat supply, supplemented by mantle heat flow. It is classified as a convective high-temperature geothermal system with a magmatic heat source. The Doma system in southern Qiangtang lies adjacent to the Bangong Co–Nujiang suture zone, where faults provide access to deep heat. Its heat sources comprise mantle heat flow and localized intracrustal melt bodies, defining a structurally controlled, deep-circulation,

high-temperature geothermal system. The Longmu Co system in northern Qiangtang lies near the Longmu Co–Shuanghu suture zone and is jointly controlled by neotectonic faulting and magmatic activity. Its heat sources comprise mantle heat flow and localized intracrustal melt bodies, defining a geothermal system controlled by tectonic and magmatic activity.

Funding: This research was supported by the Guangxi Key Technologies R&D Program (Nos.FN2600640111), the special funding for basic scientific research business expenses of the Chinese Academy of Geological Sciences (Grant Nos. JKYZD202331 and JKYQN202366), the Guangxi Natural Science Foundation (Grant No. 2026GXNSFBA00640307), and the Geological Survey Program of China Geological Survey (Grant No. DD20240200707).

References

Alçiçek H, Bülbül A, Yavuzer İ et al (2019) Hydrogeochemical and isotopic assessment and geothermometry applications in relation to the Karahayıt Geothermal Field (Denizli Basin, SW Anatolia, Turkey). Hydrogeology Journal 27(5):1791–1816. https://doi.org/10.1007/s10040-019-01927-y

Arnórsson S, Gunnlaugsson E, Svavarsson H (1983) The chemistry of geothermal waters in Iceland. III. Chemical geothermometry in geothermal investigations. Geochimica et Cosmochimica Acta 47(3):567–577. https://doi.org/10.1016/0016-7037(83)90278-8

Ba J, Gao F, Peng C et al (2022) Characteristics of nitrate and heavy metals pollution in Huixian Wetland and its health risk assessment. Alexandria Engineering Journal 61(11):9031–9042. https://doi.org/10.1016/j.aej.2022.02.045

Brown LD, Zhao W, Nelson KD et al (1996) Bright spots, structure, and magmatism in southern Tibet from INDEPTH seismic reflection profiling. Science 274(5293):1688–1690. https://doi.org/10.1126/science.274.5293.1688

Cao Y, Sun Z, Li H et al (2020) Paleomagnetism and U-Pb geochronology of Early Cretaceous volcanic rocks from the Qiangtang block, Tibetan Plateau: Implications for the Qiangtang-Lhasa collision. Tectonophysics 789:228500. https://doi.org/10.1016/j.tecto.2020.228500

Chen BB, Li SL, Pogge von Strandmann PAE et al (2023) Calcium isotopic geochemistry of geothermal systems in the tectonically active southeastern Tibetan Plateau. Science of the Total Environment 867:161534. https://doi.org/10.1016/j.scitotenv.2023.161534

Craig H (1961) Standard for reporting concentrations of deuterium and oxygen-18 in natural waters. Science 133(3467):1833–1834. https://doi.org/10.1126/science.133.3467.1833

D'Amore F, Panichi C (1985) Geochemistry in geothermal exploration. International Journal of Energy Research 9(3):277–298. https://doi.org/10.1002/er.4440090307

Ding L, Kapp P, Cai F et al (2022) Timing and mechanisms of Tibetan Plateau uplift. Nature Reviews Earth & Environment 3(10):652–667. https://doi.org/10.1038/s43017-022-00318-4

Duo J (2003) The basic characteristics of the Yangbajing geothermal field—a typical high temperature geothermal system. Engineering Sciences 5(1):42–47. https://doi.org/10.3969/j.issn.1009-1742.2003.01.008

Elenga HI, Tan H, Su J et al (2021) Origin of the enrichment of B and alkali metal elements in the geothermal water in the Tibetan Plateau: Evidence from B and Sr isotopes. Geochemistry 81(3):125797. https://doi.org/10.1016/j.chemer.2021.125797

Fisher RS, Mullican WF III (1997) Hydrochemical evolution of sodium-sulfate and sodium-chloride groundwater beneath the northern Chihuahuan Desert, Trans-Pecos, Texas, USA. Hydrogeology Journal 5(2):4–16. https://doi.org/10.1007/s100400050102

Foroutan M, Ghazanfari E, Amirlatifi A et al (2021) Variation of pore-network, mechanical and hydrological characteristics of sandstone specimens through CO_2-enriched brine injection. Geomechanics for Energy and the Environment 26:100217. https://doi.org/10.1016/j.gete.2020.100217

Fournier RO (1977) Chemical geothermometers and mixing models for geothermal systems. Geothermics 5:41–50. https://doi.org/10.1016/0375-6505(77)90007-4

Fournier RO, Potter RW II (1979) Magnesium correction to the Na–K–Ca chemical geothermometer. Geochimica et Cosmochimica Acta 43(9):1543–1550. https://doi.org/10.1016/0016-7037(79)90147-9

Fournier RO, Truesdell AH (1974) Geochemical indicators of subsurface temperature: Part 2, estimation of temperature and fraction of hot water mixed with cold water. Journal of Research of the U.S. Geological Survey 2(3):263–270

Giggenbach WF (1988) Geothermal solute equilibria. Derivation of Na–K–Mg–Ca geoindicators. Geochimica et Cosmochimica Acta 52(12):2749–2765. https://doi.org/10.1016/0016-7037(88)90143-3

Giggenbach WF (1992) Isotopic shifts in waters from geothermal and volcanic systems along convergent plate boundaries and their origin. Earth and Planetary Science Letters 113(4):495–510. https://doi.org/10.1016/0012-821X(92)90127-H

Guo N, Liu Z, Nan DW et al (2020) The characteristics and reservoir temperatures of hot springs in Jueyong, Chamdo, Xizang (Tibet). Geological Review 66(2):499–509. https://doi.org/10.16509/j.georeview.2020.02.018

Guo Q (2012) Hydrogeochemistry of high-temperature geothermal systems in China: a review. Applied Geochemistry 27(10):1887–1898. https://doi.org/10.1016/j.apgeochem.2012.07.006

Guo Q, Wang Y, Liu W (2007) Major hydrogeochemical processes in the two reservoirs of the Yangbajing geothermal field, Tibet, China. Journal of Volcanology and Geothermal Research 166(3–4):255–268. https://doi.org/10.1016/j.jvolgeores.2007.08.004

Guo Q, Wang Y, Liu W (2010) O, H, and Sr isotope evidences of mixing processes in two geothermal fluid reservoirs at Yangbajing, Tibet, China. Environmental Earth Sciences 59(7):1589–1597. https://doi.org/10.1007/s12665-009-0145-y

Han S, Nan D, Liu Z et al (2024) Hydrochemical characteristics and formation mechanism of geothermal fluids in Zuogong County, southeastern Tibet. Water 16(19):2852. https://doi.org/10.3390/w16192852

Hartanto P, Alam BYCSSS, Lubis RF et al (2022) The application of hydrogeochemical and stable isotope data to decipher the origin and evolution of hot springs in the Rawadanau Basin, Indonesia. Geothermics 105:102506. https://doi.org/10.1016/j.geothermics.2022.102506

Huang X, Huang J, Xie Y et al (2026) A comparative study of hydrochemical signatures and formation mechanisms of geothermal waters in the tensile and shear faults of the Tibetan plateau. Geothermics 135:103540. https://doi.org/10.1016/j.geothermics.2025.103540

Kapp P, Yin A, Manning CE et al (2000) Blueschist-bearing metamorphic core complexes in the Qiangtang block reveal deep crustal structure of northern Tibet. Geology 28(1):19–22. https://doi.org/10.1130/0091-7613(2000)28<19:BMCCIT>2.0.CO;2

Kapp P, Taylor M, Stockli D et al (2008) Development of active low-angle normal fault systems during orogenic collapse: Insight from Tibet. Geology 36(1):7–10. https://doi.org/10.1130/G24054A.1

Lei L, Jin S, Dong H et al (2023) 3-D electrical structure and tectonic dynamics in the Yangbajing area based on the array magnetotelluric data. Frontiers in Earth Science 10:1089675. https://doi.org/10.3389/feart.2022.1089675

Liu LX, Lu R, Xie WP et al (2024) Distribution and hydrogeochemical characteristics of hot springs in the northeastern Qinghai-Tibet Plateau. Earth Science Frontiers 31(6):173–195. https://doi.org/10.13745/j.esf.sf.2024.7.17

Liu R, He B, Zheng M et al (2020) The sedimentary evolution during Late Triassic–Jurassic period and the hydrocarbon exploration direction in the eastern part of the Qiangtang Basin, Tibet. Acta Geologica Sinica – English Edition 94(S1):35–35. https://doi.org/10.1111/1755-6724.14449

Liu X, Liu Y, Rao Y et al (2026) Cretaceous–Cenozoic tectonic evolution of the central Qiangtang terrane and implications for the initial growth of the Tibetan Plateau. Tectonophysics 918:230986. https://doi.org/10.1016/j.tecto.2025.230986

Ma N (2021) Comparison of variations in land surface evapotranspiration between typical alpine steppe and wetland ecosystems on the Tibetan Plateau over the last four decades. Advances in Earth Science 36(8):836–848. https://doi.org/10.11867/j.issn.1001-8166.2021.079

Olasolo P, Juárez MC, Morales MP et al (2016) Enhanced geothermal systems (EGS): A review. Renewable and Sustainable Energy Reviews 56:133–144. https://doi.org/10.1016/j.rser.2015.11.031

Pichler T (2005) Stable and radiogenic isotopes as tracers for the origin, mixing and subsurface history of fluids in submarine shallow-water hydrothermal systems. Journal of Volcanology and Geothermal Research 139(3–4):211–226. https://doi.org/10.1016/j.jvolgeores.2004.08.007

Ren Z, Cui J, Liu C et al (2015) Apatite fission track evidence of uplift cooling in the Qiangtang Basin and constraints on the Tibetan Plateau uplift. Acta Geologica Sinica – English Edition 89(2):467–484. https://doi.org/10.1111/1755-6724.12441

Shi Z, Tan H, Xue F et al (2024) Hydrochemical evolution and source mechanisms governing the unusual lithium and boron enrichment in salt lakes of northern Tibet. Geological Society of America Bulletin 136(11–12):5174–5190. https://doi.org/10.1130/B37516.1

Su J, Tan H, Chen X (2020) The groundwater deep circulation and large-scale geothermal deposition in response to the extension of the Yadong–Gulu rift, South Tibet, China. Journal of Volcanology and Geothermal Research 395:106836. https://doi.org/10.1016/j.jvolgeores.2020.106836

Tan H, Zhang Y, Zhang W et al (2014) Understanding the circulation of geothermal waters in the Tibetan Plateau using oxygen and hydrogen stable isotopes. Applied Geochemistry 51:23–32. https://doi.org/10.1016/j.apgeochem.2014.09.006

Wang C, Zheng M, Zhang X et al (2021) Geothermal-type lithium resources in Southern Xizang, China. Acta Geologica Sinica – English Edition 95(3):860–872. https://doi.org/10.1111/1755-6724.14675

Wang Q, Hawkesworth CJ, Wyman D et al (2016) Pliocene-Quaternary crustal melting in central and northern Tibet and insights into crustal flow. Nature Communications 7(1):11888. https://doi.org/10.1038/ncomms11888

Wang S, Xu W, Guo T (2024) Advances in thermal infrared remote sensing technology for geothermal resource detection. Remote Sensing 16(10):1690. https://doi.org/10.3390/rs16101690

Wang X, Zhang J, Jiang W et al (2019) Gravity field and deep seismogenic environment in the Longmen Shan and adjacent regions, Eastern Tibetan Plateau. Journal of Asian Earth Sciences 176:79–87. https://doi.org/10.1016/j.jseaes.2019.02.003

Wang Y, Li L, Wen H et al (2022) Geochemical evidence for the nonexistence of supercritical geothermal fluids at the Yangbajing geothermal field, southern Tibet. Journal of Hydrology 604:127243. https://doi.org/10.1016/j.jhydrol.2021.127243

Wang Y, Zhou X, Tian J et al (2023) Volatile characteristics and fluxes of He–CO_2 systematics in the southeastern Tibetan Plateau: constraints on regional seismic activities. Journal of Hydrology 617:129042. https://doi.org/10.1016/j.jhydrol.2022.129042

Wei W, Unsworth M, Jones A et al (2001) Detection of widespread fluids in the Tibetan crust by magnetotelluric studies. Science 292(5517):716–719. https://doi.org/10.1126/science.1010580

Xu G, Wu KY, Wang P et al (2020) Hydrogeochemical characteristics of the geothermal field in Wenquan basin, northern Tibet. Carsologica Sinica 39(3):299–310

Ye J, Mao X (2024) Changes in temperature and driving force during phase transition in high-temperature hydrothermal systems. Earth Science 49(10):3773–3783. https://doi.org/10.3799/dqkx.2023.126

Yin A, Harrison TM (2000) Geologic evolution of the Himalayan-Tibetan orogen. Annual Review of Earth and Planetary Sciences 28(1):211–280. https://doi.org/10.1146/annurev.earth.28.1.211

Yin A, Taylor MH (2011) Mechanics of V-shaped conjugate strike-slip faults and the corresponding continuum mode of continental deformation. Geological Society of America Bulletin 123(9–10):1798–1821. https://doi.org/10.1130/B30159.1

Yu X, Wei Z, Wang G et al (2022) Hot spring gas geochemical characteristics and geological implications of the Northern Yadong-Gulu Rift in the Tibetan Plateau. Frontiers in Earth Science 10:863559. https://doi.org/10.3389/feart.2022.863559

Zhang L, Guo Z, Zhang M et al (2017) Post-collisional potassic magmatism in the eastern Lhasa terrane, South Tibet: Products of partial melting of mélanges in a continental subduction channel. Gondwana Research 41:9–28. https://doi.org/10.1016/j.gr.2015.11.007

Zhang M, Guo Z, Xu S et al (2021) Linking deeply-sourced volatile emissions to plateau growth dynamics in southeastern Tibetan Plateau. Nature Communications 12:4157. https://doi.org/10.1038/s41467-021-24415-y

Zhang Y, Xiao Y, Yang H et al (2024) Hydrogeochemical and isotopic insights into the genesis and mixing behaviors of geothermal water in a faults-controlled geothermal field on Tibetan Plateau. Journal of Cleaner Production 442:140980. https://doi.org/10.1016/j.jclepro.2024.140980

Zhang YC, Shen SZ, Shi GR et al (2012) Tectonic evolution of the Qiangtang Block, northern Tibet during the Late Cisuralian (Late Early Permian): evidence from fusuline fossil records. Palaeogeography, Palaeoclimatology, Palaeoecology 350–352:139–148. https://doi.org/10.1016/j.palaeo.2012.06.025

Zhang Z, Deng Y, Teng J et al (2011) An overview of the crustal structure of the Tibetan plateau after 35 years of deep seismic soundings. Journal of Asian Earth Sciences 40(4):977–989. https://doi.org/10.1016/j.jseaes.2010.03.010

Zhao P, Dor J, Liang T et al (1998) Characteristics of gas geochemistry in Yangbajing geothermal field, Tibet. Chinese Science Bulletin 43(21):1770–1777. https://doi.org/10.1007/BF02883369

Zheng B, Xu J, Ni T et al (2015) Geothermal energy utilization trends from a technological paradigm perspective. Renewable Energy 77:430–441. https://doi.org/10.1016/j.renene.2014.12.035

Zheng X, Duan C, Xia B et al (2019) Hydrogeochemical modeling of the shallow thermal water evolution in Yangbajing geothermal field, Tibet. Journal of Earth Science 30(4):870–878. https://doi.org/10.1007/s12583-016-0918-7

Zhou H, Kuang X, Hao Y et al (2023) Magmatic fluid input controlling the geochemical and isotopic characteristics of geothermal waters along the Yadong-Gulu rift, southern Tibetan Plateau. Journal of Hydrology 619:129196. https://doi.org/10.1016/j.jhydrol.2023.129196